Estimating agricultural ammonia volatilization over Europe using satellite observations and simulation data

Rimal Abeed[1], Camille Viatte[1], William C. Porter[2], Nikolaos Evangeliou[3], Cathy Clerbaux[1,4], Lieven Clarisse[4], Martin Van Damme[4,5], Pierre-François Coheur[4], and Sarah Safieddine[1]

[1]LATMOS/IPSL, Sorbonne Université, UVSQ, CNRS, Paris, France
[2]Department of Environmental Sciences, University of California, Riverside, CA 92521, USA
[3]Norwegian Institute for Air Research (NILU), Department of Atmospheric and Climate Research (ATMOS), Kjeller,   Norway
[4]Université libre de Bruxelles (ULB), Spectroscopy, Quantum Chemistry and Atmospheric Remote Sensing (SQUARES), Brussels, Belgium
[5]Belgian Institute for Space Aeronomy (BIRA-IASB), Brussels 1180, Belgium

Correspondence to: Rimal Abeed   rimal.abeed@latmos.ipsl.fr

Abstract

Ammonia (NH_3) is one of the most important gases emitted from agricultural practices. It affects air quality and the overall climate, and in turn influenced by long term climate trends as well as by short term fluctuations in local and regional meteorology. Previous studies have established the capability of the Infrared Atmospheric Sounding Interferometer (IASI) series of instruments aboard the Metop satellites to measure ammonia from space since 2007. In this study, we explore the interactions between atmospheric ammonia, land and meteorological variability, and long-term climate trends in Europe. We investigate the emission potential (Γ_{soil}) of ammonia from the soil, which describes the soil – atmosphere ammonia exchange. Γ_{soil} is generally calculated in-field or in laboratory experiments; here, and for the first time, we investigate a method which assesses it remotely using satellite data, reanalysis data products, and model simulations.

We focus on ammonia emission potential during March 2011, which marks the start of growing season in Europe. Our results show that Γ_{soil} ranges from 2×10^3 to 9.5×10^4 (dimensionless) in a fertilized cropland, such as in the North European Plain, and is of the order of $10 - 10^2$ in a non-fertilized soil (e.g. forest and grassland). These results agree with in-field measurements from the literature, suggesting that our method can be used in other seasons and regions in the world. However, some improvements are needed in the determination of mass transfer coefficient k (m s^{-1}), which is a crucial parameter to derive Γ_{soil}.

Using a climate model, we estimate the expected increase in ammonia columns by the end of the century based on the increase in skin temperature (T skin), under two different climate scenarios. Ammonia columns are projected to increase by up to 50 %, particularly in Eastern Europe, under the SSP2-4.5 scenario, and might even double (increase of 100 %) under the SSP5-8.5 scenario. The increase in skin temperature is responsible for a formation of new hotspots of ammonia in Belarus, Ukraine, Hungary, Moldova, parts of Romania, and Switzerland.

1. Introduction

Ammonia (NH$_3$) emissions have been increasing in a continuous manner from 1970 to 2017 (McDuffie et al., 2020). During the period 2008 – 2018 alone, the increase in ammonia columns in Western and Southern Europe accounted to 20.8 % yr^{-1} ($\pm$ 4.3 %), and to 12.8 ($\pm$ 1.3 %) globally (Van Damme et al., 2021). Although ammonia alone is stable against heat and light, it is considered a very reactive base, whereas it constitutes the largest portion of the reactive nitrogen (N$_r$) on Earth. The vast majority of atmospheric ammonia not deposited is transformed into fine particulate matter (PM$_{2.5}$) composed of ammonium (NH$_4^+$), through acid – base chemical reactions with available acids in the environment, namely sulfuric acid (H$_2$SO$_4$), hydrochloric acid (HCl), and nitric acid (HNO$_3$) (Yu et al., 2018), while only 10 % of the total ammonia gas are believed to be oxidized by hydroxyl radicals (OH$^-$) (Roelle and Aneja, 2005). PM$_{2.5}$ has degrading effects on human health, especially respiratory diseases (Bauer et al., 2016). In addition to agriculture, ammonia can be emitted from industrial processes, biomass burning (Van Damme et al., 2018), and natural activities such as from seal colonies (Theobald et al., 2006).

Soils are known to be a source of atmospheric ammonia, especially in areas of intensive agricultural practices (Schlesinger and Hartley, 1992), and this is due to enriching the soil with the reactive nitrogen present in fertilizers. The increase in the application of synthetic fertilizers, and intensification of agricultural practices is believed to be the dominant factor of the global increase in ammonia emissions over the past century (Behera et al., 2013; McDuffie et al., 2020).

Following the application of fertilizers, ammonium and ammonia are released in the soil. Prior to its volatilization, ammonia in the soil exists either in the gas phase (NH$_{3\,(g)}$) or in the aqueous/liquid phase (NH$_{3\,(aq)}$), the equilibrium between both states of ammonia is governed by Henry's law (Wentworth et al., 2014), as shown in A. The dissociation of ammonia in soil water is affected by soil acidity (pH) and temperature (Roelle and Aneja, 2005) (Eq. (A-1) and (A-2) in Appendix A); it is explained by the dissociation constant $K_{NH_4^+}$. Once released to the atmosphere, ammonia near the surface exists is in the gas phase, hence Henry's law describes the equilibrium between ammonia in the soil (liquid phase), and near the surface (gas phase). This bi-directional exchange between the soil and the atmosphere will continue until the equilibrium is reached, and this occurs when ammonia concentration is equal to the compensation point χ_{NH_3} (the concentration of ammonia at equilibrium). The flux of ammonia from the soil to the atmosphere (emission) occurs when the concentration of atmospheric ammonia is less than the compensation point χ_{NH_3}, while ammonia deposition occurs when the concentration of ammonia is equal to or greater than χ_{NH_3} (Flechard et al., 2011; Wichink Kruit, 2010). It is then crucial to quantify the compensation point in order to understand this bi-directional exchange. The main variables needed to calculate χ_{NH_3} are soil temperature (T skin) and Γ_{soil}, which is a dimensionless ratio between ammonium and pH (NH$_4^+{}_{(aq)}$ and H$^+{}_{(aq)}$ concentrations, respectively, in the soil). All the equations are described in Appendix A (Eq. (A-1) to (A-15)).

The soil emission potential (Γ_{soil}) has been thoroughly investigated in field and controlled laboratory environments (e.g. David et al., 2009; Flechard et al., 2013; Massad et al., 2010; Mattsson et al., 2008; Nemitz et al., 2000; Wentworth et al., 2014, among others). Γ_{soil} is dimensionless and it can range from 20 (non-fertilized soil in a forest) to the order of 10^6 (mixture of slurry in a cropland). It is found to peak right after fertilizers application, due to the increase in ammonium content in the soil (a product of urea hydrolysis), reaching pre-fertilization levels 10 days following the application (Flechard et al., 2010; Massad et al., 2010). Little information exists on regional or global scales to assess the large-scale spatial variability of ammonia emission potentials.

In order to meet the needs for a growing population, agricultural practices have intensified during the period 2003 – 2019 (more fertilizer use per surface area), resulting in an increase in the net primary production (NPP) per capita

85   (Potapov et al., 2022), subsequently increasing volatilized ammonia (increase in nitrogen soil content, and
86   cultivated lands). In Europe alone, the area of croplands increased by 9 % from 2003 to 2019, and most of the
87   expansion took place on lands that were abandoned for more than 4 years (Potapov et al., 2022). Between the year
88   2008 and 2018, the increase in atmospheric ammonia columns accounted to 20.8 % (± 4.3 %) in Western and
89   Southern Europe (Van Damme et al., 2021). With the increase in croplands area and agricultural activities, climate
90   change will have a significant effect on agricultural practices, with warmer climates enhancing the volatilization
91   of ammonia from soils, especially in intensely fertilized lands (Shen et al., 2020).
92
93   This study aims at exploring ammonia emission potential/volatilization in Europe, using infrared satellite data of
94   ammonia columns, reanalysis temperature data, and chemical transport model simulations to provide information
95   on chemical sources and sinks. We specifically study the relationship between satellite-derived ammonia
96   concentration at the start of the growing season, soil emission potentials and their spatial variability over Europe
97   during March of 2011. Section 2 provides the methods/datasets used. Simulation results are described in Sect. 3,
98   and regional emission potentials are shown and discussed in Sect. 4. Using a climate model, future projections of
99   ammonia columns are investigated under different climate scenarios in Sect. 5. Discussion and conclusions are
100   listed in Sect. 6.

2. Methodology

2.1. Calculation of the emission potential

104   In this study, we use IASI satellite data to calculate the ammonia emission potential Γ_{soil} instead of field soil
105   measurements. In field studies, Γ_{soil} is calculated by measuring the concentration of ammonium (NH_4^+) and H^+
106   (10^{-pH}) in the soil; the ratio between both of these concentrations is Γ_{soil}. In this study, we use infrared satellite
107   ammonia to have a regional coverage over Europe. With these, we cannot monitor soil content of ammonium nor
108   its pH. This renders the remote Γ_{soil} calculation challenging, and less straight forward. The full derivation of the
109   equation used to calculate the emission potential is explained in Appendix A, and was briefly described in the
110   introduction. In short, upon its dissolution in the soil water, ammonia follows Henry's law. In steady state
111   conditions between the soil and the near surface, the amount of the ammonia emitted and lost is considered equal.
112   Based on this assumption, the soil emission potential (dimensionless) is calculated as follows Eq. (2-1) or Eq. (A-
113   15) in Appendix A:

$$\Gamma_{soil} = \frac{[NH_3]^{col} \cdot T_{soil}}{\exp(\frac{-b}{T_{soil}})} \frac{M_{NH_3}}{a \cdot N_a \cdot c'} \cdot \frac{1}{k\tau} \tag{2-1}$$

116   Where $[NH_3]^{col}$ is the total column concentration of ammonia (molecules cm^{-2}), measured by satellite remote
117   sensors, T_{soil} is the soil temperature at the surface, which can be expressed as the skin temperature, T skin (Kelvin),
118   a and b are constants ($a = 2.75 \times 10^3$ g K cm^{-3}, $b = 1.04 \times 10^4$ K), M_{NH_3} is the molar mass of ammonia gas
119   ($M = 17.031$ g mol^{-1}), and N_a is Avogadro's number ($N_a = 6.0221409 \times 10^{23}$ $molecules$ mol^{-1}), c' is
120   equals to 100 and is added to convert k from m s^{-1} to cm s^{-1} (since $[NH_3]^{col}$ is in molecules cm^{-1}), and τ the lifetime
121   of ammonia (seconds).
122   k is the soil – atmosphere exchange coefficient or deposition velocity (cm s^{-1}), also known as the mass transfer
123   coefficient (this nomenclature will be used in this study). It is found to be affected by the roughness length of the
124   surface, wind speed, the boundary layer height (Olesen and Sommer, 1993; Van Der Molen et al., 1990), and pH

125 (Lee et al., 2020). It can be explained by a resistance model often used to explain the exchange between the surface
126 and the atmosphere (Wentworth et al., 2014). Different studies provide look up tables values of k for different land
127 cover types and different seasons based on this resistance model (Aneja et al., 1986; Erisman et al., 1994; Phillips
128 et al., 2004; Roelle and Aneja, 2005; Svensson and Ferm, 1993; Wesely, 1989).
129 In general, the mass transfer coefficient k is in the order of 10^{-3} to 10^{-2} m s^{-1} in a mixture of soil and manure, and
130 10^{-6} to 10^{-5} m s^{-1} in a mixture of manure alone (Roelle and Aneja, 2005). We discuss and provide more information
131 on k in Sect. 4, and additional details on this calculation in general are provided in Appendix A.
132

2.2. IASI ammonia, ERA5 T skin, and MODIS Land cover

134
135 The Infrared Atmospheric Sounding Interferometer (IASI) is considered advanced the most innovative
136 instrument onboard the polar-orbiting Metop satellites (Klaes, 2018). Three IASI instruments are onboard Metop-
137 A, B and C, the series of satellites launched by the EUMETSAT (European Organization for the Exploitation of
138 Meteorological Satellites) in 2006, 2012, and 2018, respectively. The Metop-A satellite was de-orbited in October
139 2021 (Lentze, 2021), and as a result only two instruments (IASI-B and C onboard Metop-B and C) are operating
140 today. The observations from IASI cover any location on Earth at 9:30 in the morning (AM) and in the evening
141 (PM), local solar time. It can detect a variety of atmospheric species including trace gases (Clerbaux et al., 2009).
142 The IASI Fourier-transform spectrometer monitors the atmosphere in the spectral range between 645 and 2760
143 cm^{-1} (thermal infrared), and is nadir-looking. IASI has a swath width that measures 2200 km, with a pixel size of
144 ~12 km.
145
146 Ammonia was first detected with IASI using the υ_2 vibrational band of ammonia (~950 cm^{-1}) (Clerbaux et al.,
147 2009; Coheur et al., 2009). The ammonia total columns used in this study are the product of an Artificial Neural
148 Network and re-analyzed temperature data from the European Centre for Medium-Range Weather Forecasts
149 (ECMWF) product ERA5 ANNI-NH$_3$-v3R-ERA5 (Van Damme et al., 2021). Several studies used ammonia data
150 from IASI to study hotspots of ammonia of different source types including both natural and anthropogenic sources
151 (Clarisse, Van Damme, Clerbaux, et al., 2019; Clarisse, Van Damme, Gardner, et al., 2019; Dammers et al., 2019;
152 Van Damme et al., 2018, 2021; Viatte et al., 2021). Recently, IASI observations were used to study the effect of
153 war and conflict on agricultural practices in Syria (Abeed et al., 2021).
154
155 Fewer errors on the retrieval were observed during the day and over land (Van Damme et al., 2017), hence, we
156 use only daytime ammonia measurements from IASI. Comparisons with ammonia measured using a ground-based
157 instrument showed a good correlation of R=0.75 (Viatte et al., 2021). Satellite ammonia data from CrIS (Crosstrack
158 Infrared Sounder) (Shephard and Cady-Pereira, 2015) were compared with those from IASI, and were equally
159 found to give similar results when looking at concentrations from a wildfire (Adams et al., 2019), showing
160 consistency when studying seasonal and inter-annual variability (Viatte et al., 2020).
161
162 In addition to ammonia, we look at skin temperature (T skin or land surface temperature LST) data from the
163 ECMWF reanalysis (ERA5) at a grid resolution of 0.25 × 0.25 ° (Hersbach et al., 2020). ERA5 Temperatures are
164 interpolated temporally and spatially to the IASI morning overpass (~9:30 A.M. local time), since we only consider
165 daytime ammonia. ERA5 temperature data are also used in the retrieval process of the ammonia data we used in
166 this study NH$_3$-v3R-ERA5 (Van Damme et al., 2021). T skin is defined as the temperature of the uppermost surface
167 layer when radiative equilibrium is reached. It also represents the theoretical temperature required in order to reach
168 the surface energy balance (ECMWF, 2016).
169

170   In order to assign a mass transfer coefficient k to each land type, the moderate resolution imaging
171   spectroradiometer (MODIS), a series of instruments orbiting the Earth aboard the Aqua and Terra satellites, is
172   used. The data product MCD12Q1 (version 6) is a combined Aqua/Terra Land cover type product, with a spatial
173   resolution of 500 m. This product provides maps of land cover type from 2001 through 2019 (Sulla-Menashe and
174   Friedl, 2018). From the land use categories included in the MOD12Q1 product (Belward et al., 1999) we focus on
175   croplands, forests, shrublands, and grasslands. We do not include barelands, snow cover, and urban areas in our
176   analysis; we are not interested in studying these surfaces, since we focus on ammonia volatilization from the soil
177   in areas amended with fertilizers. We show the emission potential in Forests and grasslands/shrublands for
178   comparison with values in the literature. In an attempt to calculate an emission potential (Eq. (2-1)) that is relevant
179   to the land cover/use, we therefore assign a mass transfer coefficient k to each land type based on literature values
180   (Aneja et al., 1986; Erisman et al., 1994; Roelle and Aneja, 2005; Svensson and Ferm, 1993; Wesely, 1989) and
181   we discuss it in Sect. 4.
182

2.3. Model simulations

2.3.1. GEOS-Chem Chemistry Transport Model

185
186   In this study we use version 12.7.2 of the GEOS-Chem chemical transport model (Bey et al., 2001). The model is
187   driven by the Modern-Era Retrospective Analysis for Research and Applications version 2 (MERRA-2) reanalysis
188   product, including nested domains over Europe at a $0.5° \times 0.625°$ horizontal resolution. MERRA-2 is the second
189   version of the MERRA atmospheric reanalysis product by NASA Global Modulation Assimilation Office
190   (NASA/GMAO) (Gelaro et al., 2017). Boundary conditions for the nested domains are created using a global
191   simulation for the same months at $2° \times 2.5°$ resolution. We generate model output for March of 2011, preceded by
192   a one month of discarded model spin-up time for the nested run, and two months for the global simulation. March
193   corresponds well to the month of fertilizer application in Europe, and as such to the beginning of the growing
194   season (FAO, 2022; USDA, 2022).
195
196   Output includes the monthly mean for selected diagnostics. Anthropogenic emissions are taken primarily from the
197   global Community Emissions Data System (CEDS) inventory (Hoesly et al., 2018). Biogenic non-agricultural
198   ammonia, as well as ocean ammonia sources, are taken from the Global Emission Inventories Activities database
199   (GEIA, (Bouwman et al., 1997)). Open fire emissions are generated using the GFED 4.1s inventory (Randerson et
200   al., 2015). We used the Harmonized Emissions Component module (HEMCO) to obtain the ammonia emissions
201   over Europe (Keller et al., 2014).
202

2.3.2. EC-Earth Climate model

204   To analyze how future climate will affect ammonia concentration and emission potential, we use the ECMWF
205   climate model the European Earth Consortium climate model (EC-Earth, http://www.ec-earth.org/). While other
206   climate models exist, we choose this one because the ammonia product from IASI uses ERA5 for the retrievals
207   and we calculate the emission potential from the T skin product of ERA5. The reanalysis uses the ECMWF
208   Integrated Forecasting System for the atmosphere–land component (IFS). IFS is also used in EC-Earth and is
209   complemented with other model components to simulate the full range of Earth system interactions that are
210   relevant to climate (Döscher et al., 2021). We note that the versions of the IFS models used in ERA5 and in EC-
211   Earth are not identical as the climate model product is not assimilated and is not initialized with observations

212 several times a day like ERA5. The EC-Earth simulations are included in the Climate model intercomparison
213 project, phase 6 (Eyring et al., 2016), part of the Intergovernmental Panel on Climate Change (IPCC) report of
214 2021 (Masson-Delmotte, et al., 2021). We use the so-called Scenario Model Intercomparison Project
215 (ScenarioMIP), covering the period [2015 – 2100] for future projections under different shared socio-economic
216 pathways (SSP) (Riahi et al., 2017). We analyze two scenarios, the SSP2-4.5 corresponding to "middle of the
217 road" socio-economic family with a nominal 4.5W/m^2 radiative forcing level by 2100 - approximately
218 corresponding to the RCP-4.5 scenario, and the SSP5-8.5 marks the upper edge of the SSP scenario spectrum with
219 a high reference scenario in a high fossil-fuel development world throughout the 21st century.

220 **3. GEOS-Chem model simulation: validation and analysis**

221 **3.1. GEOS-Chem validation with IASI**

222
223 In order to analyse how well the model simulates atmospheric ammonia, we use the simulated GEOS-Chem
224 monthly averaged (March 2011) ammonia total columns output (Sect. 2.3.1). We compare those to the IASI total
225 columns of ammonia gridded on the same horizontal resolution (0.5° × 0.625°) and over the same month.
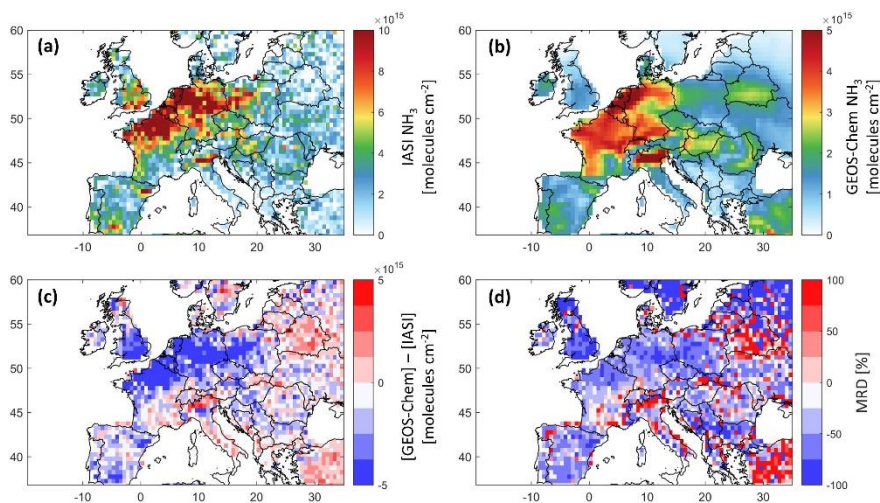

Figure 1. Ammonia total column concentrations from IASI (panel a), and GEOS-Chem (panel b), the difference between both datasets (panel c) in molecules cm^{-2}, and the Mean Relative Difference (MRD) in % (panel d); all data are a monthly average of March 2011, and over Europe at a 0.5° × 0.625° grid resolution. Note that the colour bar limits are different between panels (a) and (b).

226
227 Figure 1 shows the IASI NH$_3$ distribution (Figure 1a), and that from GEOS-Chem (Figure 1b), the bias between
228 the two (Figure 1c), and the mean relative difference MRD (Figure 1d), all during March 2011. MRD is calculated
229 as the mean of the ratio $\frac{(GeosChem\ NH_3 - IASI\ NH_3) \times 100}{IASI\ NH_3}$ at each grid point.
230

231 Generally, both GEOS-Chem and IASI show coincident sources of ammonia, reflecting the good ability of the
232 model to reproduce ammonia columns over major agricultural source regions in Europe. The bias between IASI
233 and GEOS-Chem and the MRD are shown in Figure 1c and d. Ammonia columns from GEOS-Chem are
234 underestimated by up to 2×10^{16} molecules/cm² in some source regions/over hotspots, especially in England, North
235 Eastern France, the North European Plain (Netherlands, Belgium), and Spain (around Barcelona). Similar results
236 were found in the study of Whitburn et al. (2016), in which they show that GEOS-Chem underestimates ammonia
237 columns by up to 1×10^{16} molecules/cm² in Europe on a yearly average in 2009, notably in the North European
238 Plain. It is important to note that, in our study, we compare only one month of data (March, 2011) that marks the
239 start of the growing season in the majority of the countries of interest (FAO, 2022; USDA, 2022). The differences
240 are mainly because of the time coincidence, and the fact that only cloud-free data are used to retrieve ammonia;
241 IASI observes ammonia during the satellite overpass (~9:30 AM local time), whereas the GEOS-Chem simulation
242 is averaged over the whole month including all hours of the day. In Western and Northern Europe, the MRD is
243 mostly less than −50 %, for instance, in the North European Plain (−49 %). If we look at the average MRD in
244 regions of focus, we see that the Po Valley in Italy has the highest MRD value (+110 %), whereas the best
245 represented region is New Aquitaine in the southwest of France (−20 %). The rest of the regions have mean MRDs
246 that fluctuate between −64 % and – 42 %. A summary of the results of this study, including the MRD over some
247 source regions is listed in Table 1. Although the bias and MRD can be considered high, the spatial distribution is
248 consistent between IASI and GEOS-Chem. Therefore, according to the steady state approximation, the
249 meteorological and soil parameters affecting one dataset (e.g. IASI NH_3) are applicable to the other (e.g. model
250 simulation). It is worth noting that although we do not use the latest version of GEOS-Chem, the results we obtain
251 reflects our current understanding of the regional chemistry at this horizontal and temporal resolution.

3.2. Ammonia emissions, losses and lifetime in Europe

253 In order to understand the NH_3 spatial variability in Europe during the application of fertilizers, a detailed analysis
254 of the output of the GEOS-Chem simulation for the month of March 2011 is shown in Figure 2.
255 The anthropogenic sources (i.e. mainly agriculture) contribute 83 % of the total ammonia emissions during March
256 2011 in Europe. The ammonia emissions from natural sources (i.e. soil of natural vegetation, oceans, and wild
257 animals) follow representing 16 % of the total emissions, whereas the remaining 1 % correspond to the ammonia
258 emissions from biomass burning and ships (not shown here).
259 Figure 2a shows ammonia monthly emissions. Most of them are due to agricultural activities (not shown here); we
260 identify 8 source regions which we investigate thoroughly in this study shown as rectangles A to H. The highest
261 agricultural sources over Europe include the North European Plain, Brittany, and the Po Valley (regions C, D, and
262 F).
263 In the calculation of the total loss of ammonia (Figure 2b), we considered dry deposition, chemistry, transport, and
264 wet deposition (in which we included ammonia loss to convection) from the GEOS-Chem model simulation, which
265 are all possible loss processes for ammonia (David et al., 2009). Figure 2b shows that the largest losses occur
266 logically where we have the highest sources detected (see Figure 2a).
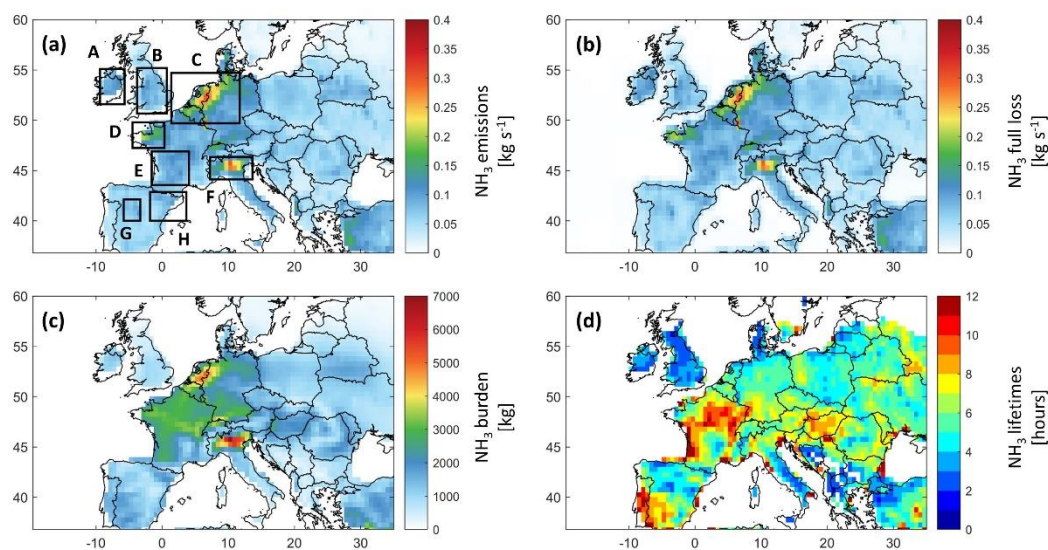267
268

Figure 2. Ammonia budget in Europe from GEOS-Chem: (a) Ammonia emissions from the Harmonized Emissions Component module (HEMCO) in kg s⁻¹ with our regions of interest shown in rectangles, (b) ammonia full loss in kg s⁻¹, (c) ammonia total burden in kg, and (d) ammonia lifetime in hours. All plots refer to March 2011 and are presented at a $0.5° \times 0.625°$ grid resolution.

269   The total ammonia burden (Figure 2c) is calculated as the integrated sum of all ammonia columns in the model
270   grid box. We can clearly detect ammonia hotspots over Europe, in particular the North European Plain, Brittany
271   and the Po Valley, all regions characterized by intense agricultural activities, as the total emissions and deposition
272   show (Figure 1 and Figure 2). We also see that the burden is generally the highest over France, Belgium, The
273   Netherlands, and parts of Germany and Italy.
274
275   We finally get the lifetime τ_{ss} of ammonia (Figure 2d). In the case of a gas with a short lifetime, such as ammonia,
276   the emissions are relatively well-balanced spatially by eventual sinks/losses (steady-state approximation).
277   Therefore, we can calculate a steady-state lifetime as the ratio between the total burden B (Figure 2c) and the total
278   emissions E or losses L (sum of all emitted / lost molecules, Figure 2a or b) using the following equation: $\tau_{ss} =$
279   B/L (Plumb and Stolarski, 2013).
280
281   We note that the τ_{ss} is more or less the same whether we calculate it using the losses or the emissions. For instance,
282   in selected source regions (rectangles in Figure 2a) the total emissions and losses are very close with very low
283   biases that are less than 2% (not shown here). Our results show that τ_{ss}, on a monthly average, can go up to 12
284   hours, and it can reach 1 day (24 hours) in coastal regions such as region E in New Aquitaine in France. The latter
285   can be related to the high probability of air stagnation is in that area in comparison to Northern Europe (Garrido-
286   Perez et al., 2018), since higher PM$_{2.5}$ pollution episodes were found under stagnant meteorological conditions
287   (AQEG, 2012); and ammonium molecules carried on these PM$_{2.5}$ can transform back into ammonia. Our results
288   agree with the literature suggesting a residence time between a few hours to a few days (Behera et al., 2013; Pinder
289   et al., 2008), and with those calculated by Evangeliou et al. (2021) over Europe, showing a monthly average of
290   ammonia lifetime that ranges from 10 to 13 hours in Europe. The figure adapted from Evangeliou et al. (2021) is

291   shown in supplementary material (Figure S1). Shorter lifetimes from industrial sources of ammonia were reported
292   in Dammers et al. (2019), with a mean lifetime of ammonia that is equal to 2.35 hours (±1.16). A recent study
293   found lifetimes of ammonia that vary between 5 and 25 hours, roughly, in Europe (Luo et al., 2022); these values
294   are higher since, in addition to ammonia loss, Luo et al. (2022) included the loss of ammonium, and thus
295   considering the loss of ammonia only terminal when the ammonium is also lost/deposited. This approach is not
296   considered here nor in Evangeliou et al. (2021).

298   Notably, ammonia lifetime and burden (Figure 2c, and d) each have different spatial distribution compared to the
299   other 2 panels (Figure 2a, and b). The ammonia residence time in the atmosphere varies depending on the sources
300   and more importantly on the locally dominant loss mechanisms. For this reason, in Figure 3, we show the relative
301   contribution of the ammonia loss mechanisms, presented as pie charts, for the agricultural source regions shown
302   in black boxes in Figure 2a.

304   The fastest loss mechanisms are either chemical (i.e. in the vast majority transformation to particulate matter) or
305   through wet and dry deposition (Tournadre et al., 2020). Figure 3 shows that more than 50 % of the ammonia
306   molecules in the atmosphere are lost to chemical reactions in most of the regions (A, B, C, H, and F). The shortest
307   residence time of ammonia is observed in England, where the chemical removal was significantly higher than
308   other sinks and represented up to 73 % of the total ammonia loss pathways, suggesting a rapid transformation into
309   inorganic particulate matter ($PM_{2.5}$). In the regions D, G and E the chemical loss makes up 50 %, 49 %, and 42 %,
310   respectively. In fact, in March 2011, PM was found to be mostly composed of inorganic nitrate (41 %), and
311   ammonium (20 %) (Viatte et al., 2022) over Europe, both of which are products of atmospheric ammonia. Nitrate-
312   bearing $PM_{2.5}$ are formed when nitric acid (HNO_3) reacts with ammonia (Yang et al., 2022), and ammonium is a
313   direct product of the hydrolysis of ammonia. 41% of the nitric acid formed in the atmosphere is produced from the
314   reaction between nitrogen dioxide (NO_2) and the hydroxyl radical (OH) (Alexander et al., 2020). These chemical
315   pathways help explain the large chemical losses in most of the regions studied in Figure 3.

317   Ammonia loss to transport is the highest in regions neighboring the Atlantic Ocean, accounting for 30 %, 27 %,
318   32 %, and 34 % of total sinks in regions A, D, E, and G respectively. These regions are exposed to the North
319   Atlantic Drift, also known as the Gulf Stream, that is associated with high wind speed and cyclonic activity (Barnes
320   et al., 2022). In other regions, 14 % to 22 % of the total ammonia is lost to transport mechanisms, and in all regions,
321   11 to 22 % is lost to dry deposition (Figure 3). During March, precipitation is relatively lower as compared to
322   winter (December, January, February) in Europe. Furthermore, 2011 was a particular dry year compared to the
323   1981 – 2010 average (Met Office, 2016). Drought was reported to be severe in areas such as France, Belgium and
324   the Netherlands, and moderate in England and Ireland (EDO, 2011). This can help explain the low percentage of
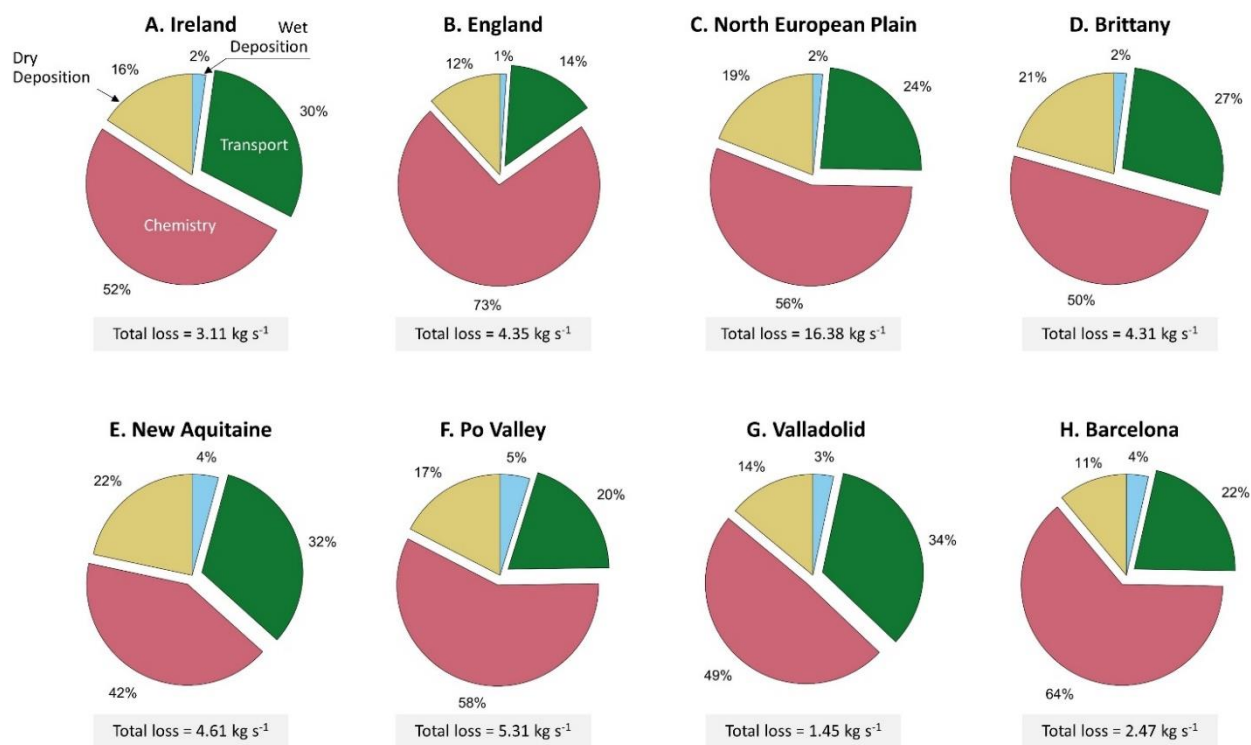325   wet deposition during March 2011 (1 to 5 % out of the total loss of ammonia).

Figure 3. Repartition of the ammonia loss mechanisms for major agricultural areas in Europe, during March 2011, as retrieved from GEOS-Chem, with the total ammonia loss shown in a grey box under each pie chart (kg s^{-1}). The regions are shown in black boxes in Figure 2a.

326

4. Ammonia emission potential over Europe

328

329 To calculate emission potential, a calculation of the mass transfer coefficient k, which relates to the land type, is
330 necessary. Figure 4 shows the land cover type from MODIS in Europe (left panel), and the corresponding assigned
331 mass transfer coefficient k (right panel) needed to calculate the emission potential (Eq. (2-1)). In order to choose
332 a mass transfer coefficient that is convenient for the different land types relevant to this study, we searched for k
333 values in the literature. Not all land types have been studied for ammonia transfer coefficient.
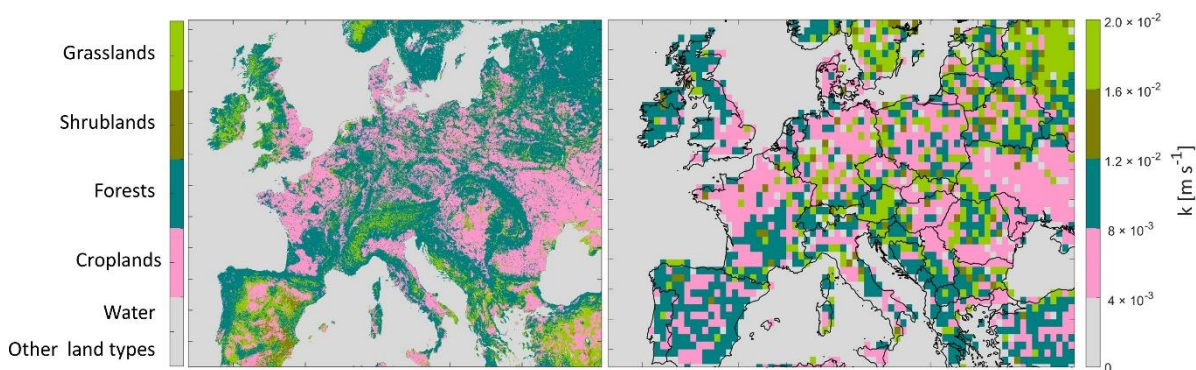334 For water bodies and other land types that are not considered here (see Sect. 2.2), the mass transfer values k were
335 set to zero and represented in grey colour in Figure 4. In a laboratory experiment, Svensson et al. (1993) reported
336 $k = 4.3 \times 10^{-3}$ m s^{-1} for a mixture of soil and swine manure, as therefore, we assign this value to croplands. Due
337 to the lack of k values for non-fertilized forests, shrublands and grasslands in the literature, we used values
338 originally assigned for SO$_2$, bearing in mind that these are approximate values and they reflect mostly the
339 conditions of the soil cover type (short, medium or tall grass). To assign a k value for forests, we used values
340 reported in Aneja (1986) ($k = 2 \times 10^{-2}$ m s^{-1}), which originally represent deposition velocity (mass transfer) of

341 SO$_2$ in a forest (high crops). For shrublands and grasslands (the two land types have the same k), we used the value
342 $k = 8 \times 10^{-3}$ m s^{-1} that has been reported in Aneja et al. (1986) as the deposition velocity (mass transfer) of SO$_2$
343 in a grassland (medium crops). These values are the best attempt to test the validity of using MODIS and lookup
344 tables of k values to calculate a realistic soil emission potential. As a result, Figure 4 (left panel) includes 5 land
345 types, while k values are reported for 4 land types (other land type/water, croplands, forests, and
346 shrublands/grasslands).
347
348 After choosing the k values, we assigned them for each land type on the (500 m $\times$ 500 m) grid. We then extrapolate
349 the array with the k values from 500 m $\times$ 500 m to the resolution of GEOS-Chem (0.5° $\times$ 0.625° grid box). This
350 leads to averaging different fine pixels with different land cover types into a coarser grid. The result is shown on
351 the right panel of Figure 4.
352

353

Figure 4. MODIS Land Cover Type, at a 500 m $\times$ 500 m grid box (left panel), and interpolated mass transfer coefficient k on a horizontal resolution of 0.5° $\times$ 0.625° grid box (right panel).

354 Uncertainties of this methodological approach can be summarized as follows:
355 (1) The k value assigned for croplands is approximate and therefore not the same in every cropland over
356   Europe.
357 (2) The k value assigned for forests represents the SO$_2$ exchange in high croplands, and ammonia might
358   change especially when the latter is highly affected by humidity; it can easily dissolve in the water film
359   on leaves in high humid conditions.
360 (3) The extrapolation of a fine array (500 m $\times$ 500 m) will merge several grids together and average them in
361   order to construct the coarser grid box (0.5° $\times$ 0.625°); the result is therefore an average that might mix
362   croplands with neighboring forests/barelands/grasslands. This leads to a range of different k values that
363   are shown on Figure 4.
364
365 Using the land-type specific k value is necessary in order to reflect realistic emissions potential, as ammonia
366 exchange in a forest is different from that of croplands or unfertilized grasslands, due to different barriers (long,
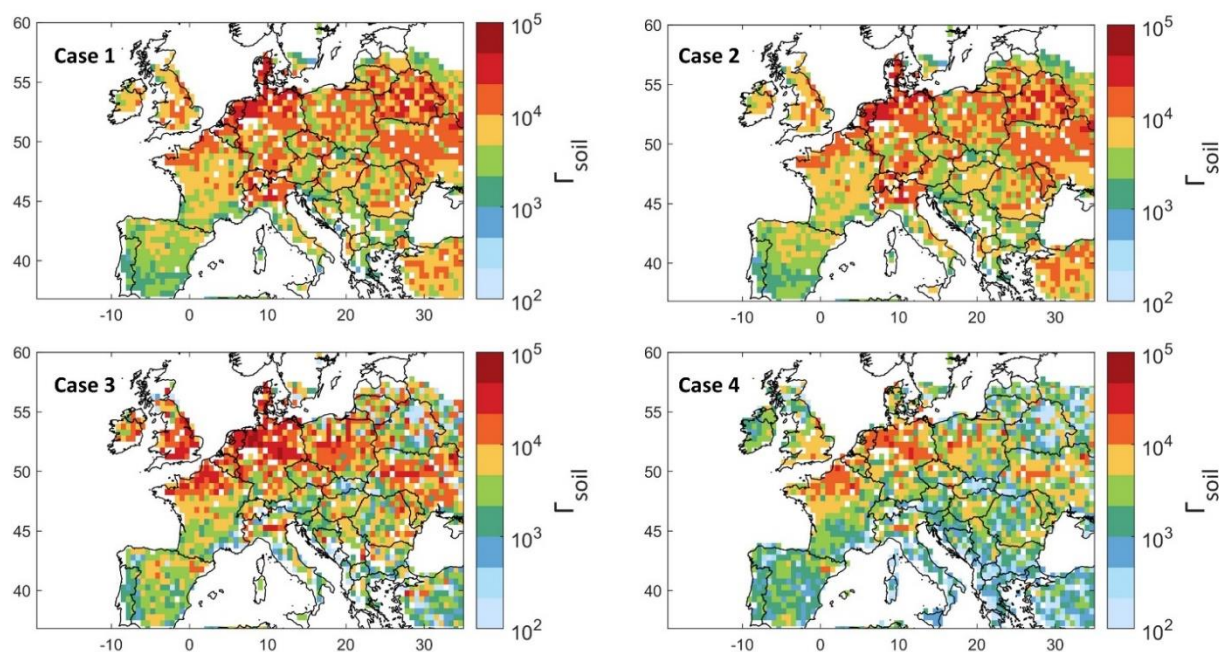367 medium or short crop / grass), and ammonium soil content in each land type.

Figure 5. Ammonia soil emission potential (Γ_{soil}) on a log10 scale from model simulation, observation and reanalysis for 4 different cases (see text for details).

368
369 We show in supplementary material Figure S2, the emission potential (similarly to what we show in Figure 5) but
370 from a fixed and averaged k value for all land types. Figure S2 shows the importance of using a variable k that is
371 adjusted to each land type is depicted in supplementary materials (Figure S2). In Figure S2, the fixed k used is
372 calculated assuming 14 days of fertilization ($k = 10^{-3}$ m s^{-1}), 7 days when k value reduces ($k = 10^{-5}$ m s^{-1}), and
373 10 days when k is low ($k = 10^{-6}$ m s^{-1}) resulting in average of $k = 4.5 \times 10^{-4}$ m s^{-1}. The difference in the
374 emission potential between fixed and spatially variable k is shown in supplementary material Figure S3, where we
375 see that a fixed k might overestimate Γ_{soil} by 10 to 10^3 on a log10 scale (500 – 3000 %), in agricultural areas.
376
377 Figure 5 illustrates the ammonia soil emission potential Γ_{soil} calculated using Eq. (2-1) and k values presented in
378 Figure 4. After assigning the variable mass transfer coefficient, the remaining variables needed to calculate Γ_{soil}
379 in Eq. (2-1) are ammonia concentration and lifetime, as well as the skin temperature. For this reason, the emission
380 potential Γ_{soil} shown in Figure 5 is calculated using different configurations.
381
382   -   Case 1: GEOS-Chem ammonia and lifetime with MERRA-2 T skin, i.e. simulated Γ_{soil},
383   -   Case 2: GEOS-Chem ammonia and lifetime and ERA5 Tskin, to check the effect of using ERA5 vs
384   MERRA-2 for skin temperature,
385   -   Case 3: IASI ammonia, ERA5 T skin and GEOS-Chem ammonia lifetime,
386   -   Case 4: IASI ammonia, ERA5 T skin and ammonia lifetime from Evangeliou et al. (2021), that were
387   calculated using LMDz-OR-INCA chemistry transport model. The latter couples three models: The
388   general circulation model GCM (LMDz) (Hourdin et al., 2006), the INteraction with Chemistry and

389   Aerosols (INCA) (Folberth et al., 2006), and the land surface dynamical vegetation model (ORCHIDEE)
390   (Krinner et al., 2005).

391

392 Based upon the four cases, we calculate a range of emission potentials. When calculating $\Gamma_{soil,}$ we filtered data
393 points with ammonia total column concentration less than 5×10^{14} molecules cm^{-2}. The latter are mostly grid boxes
394 concentrated above 56° North that we consider as noise (shown in white pixels on Figure 5).

395

396 T skin from ERA5 and MERRA-2 agree very well, with a coefficient of determination $r^2 = 0.97$ (Figure S4 in the
397 supplementary material). This explains the excellent spatial correlation between cases 1 and 2. Since IASI-NH$_3$
398 retrievals use ERA5 T skin, this also suggests that using MERRA-2 or ERA5 does not affect our Γ_{soil} calculation.
399 In case 3, the emission potential agrees spatially and in value with that of GEOS-Chem. However, we observe
400 higher Γ_{soil} in regions such as Ireland, England, North France, Northeastern Spain, and Poland. This is due to the
401 underestimation/overestimation of ammonia from GEOS-Chem as compared to IASI observations (Figure 1a). For
402 instance, Γ_{soil} from IASI and ERA5 (case 3) differs with that from GEOS-chem and ERA5 (case 2) by up to -70
403 % in the Po Valley (Italy) and +60 % in England. Looking at Table 1, this difference can be explained by the
404 corresponding MRD for each of the regions, in which it is -64 % for England and +110 % for the Po Valley.
405 Similarly, the differences between case 3 and 4 reach up to +66 % in England, and this is mostly due to the 10-
406 hours difference between ammonia lifetime from GEOS-Chem and Evangeliou et al. (2021) (Figure S1 in the
407 supplementary material). The lowest Γ_{soil} were obtained in case 4, due to the higher lifetimes than those calculated
408 from GEOS-Chem (Figure S1); note that Γ_{soil} is inversely proportional to ammonia lifetime (Eq. (2-1). In fact, the
409 longer ammonia stays in the atmosphere (longer lifetime), the less the flux will be directed from the soil to the
410 atmosphere (less ammonia emission).

411

412 In the four cases presented in Figure 5, we see similar spatial distribution of ammonia emission potential ranging
413 from 12×10^{-1} in a forest to 9.5×10^4 in a cropland (monthly average considering all the cases). In agricultural
414 lands, our results show that Γ_{soil} ranges from 2×10^3 to 9.5×10^4. Our values for croplands start at around 10^3. In
415 fact, most of the studies summarized in Zhang et al. (2010) reported Γ_{soil} that range mostly from 10^3 to 10^4 in
416 fertilized croplands/grasslands; the minimum Γ_{soil} reported is in the order of 10^2 and the maximum is of the order
417 of 10^5. Therefore, our values fit within the range of Γ_{soil} calculated in the literature and summarized in Zhang et
418 al. (2010) and the references within. Personne et al. (2015) focused on Grignon, an agricultural region near Paris,
419 France (48°51′N, 1°58′E). They obtained Γ_{soil} values between 1.1×10^4 to 5.8×10^6. In the present study, the
420 emission potential over this region is between 5×10^3 (case 4) to 2×10^4 (case 2). In this study, it is expected to
421 obtain lower values than the ones measured over specific field. Therefore, we consider our results to be in good
422 agreement with the obtained values in Personne et al. (2015), since ours reflect an average of a coarse patch of
423 land of the size 55×70 km^2 approximately, with a 31-day mean.

424

425 The mean emission potentials per ammonia source region in Europe (shown in rectangles in Figure 2 and Figure
426 3) and per case are shown in Figure 6, and listed in Table 1. Table 1 shows the average lifetime from GEOS-Chem
427 (hours), the average T skin from the three datasets that we used (°C), the average ammonia emission potential in
428 all the cases examined (dimensionless), and the average ammonia columns from IASI and GEOS-Chem
429 (molecules cm^{-2}). The four cases show a similar pattern with the North European Plain exhibiting the highest
430 emission potential. This has been shown in Figure 1, Figure 2, and Figure 5, as well as in Table 1, where Γ_{soil} is
431 higher in regions with high ammonia columns. This is expected in fertilized lands (croplands), since Γ_{soil} is
432 proportional to the concertation of ammonia near the surface. The latter increases when the soil content in
433 ammonium (NH$_4^+$) increases following the application of nitrogen-based fertilizers.

434

435 Figure 6 also shows that for cases 1 and 2 (GEOS-Chem) the emission potential in the Po Valley is higher as
436 compared to case 3 (IASI), although it stays within the margin of error. This is due to the effect of temperature.
437 Table 1 shows that at the time of the IASI overpass, T skin from ERA5 in the Po Valley is almost twice as large
438 (8.95 °C) as the monthly averaged temperature (4.46 °C). The effect of skin temperature through Eq. (2-1) makes
439 the emission potential highly dependent. In fact, Γ_{soil} is both directly and inversely proportional to T skin, however,
440 the exponential in the denominator has ~10 times more effect on the value of Γ_{soil} than the T skin in the numerator.
441 Therefore, through Eq. (2-1), we conclude that an increase in temperature by 1°C will reduce Γ_{soil} by around −8%.
442
443 The standard deviation (shaded area) is found to be the highest in the North European Plain, which is also the
444 largest region (hence higher variability is expected), especially when considering case 3 with IASI. IASI
445 distinguishes different source sub-regions, leading to higher spatial variability of ammonia, and therefore Γ_{soil}. As
446 Figure 5 has shown, case 4 has the lowest Γ_{soil}, with a factor of two lower than cases 1 to 3. This is due to the
447 longer lifetimes calculated by Evangeliou et al. (2021). However, we note that all the regions exhibit the same
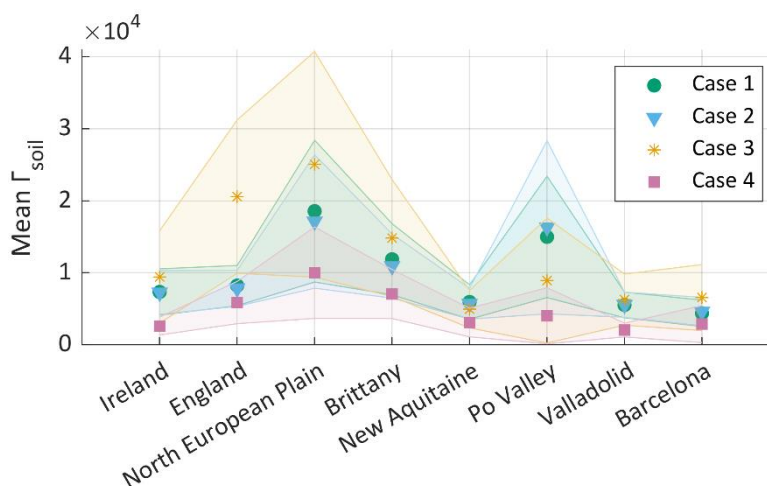448 inter-variability between each of the case, regardless of the lifetimes used.
449

Figure 6. Mean ammonia emission potential Γ_{soil} per region and per case, with the error margin on the mean as the shaded area (95th percentile) for cases 1 to 4. The cases are explained in Figure 5 and its discussion.

450
451
452
453
454
455
456
457
458
459
460

Table 1. Summary of NH$_3$ average lifetime, emission potential, concentrations and the T skin in selected regions in Europe.

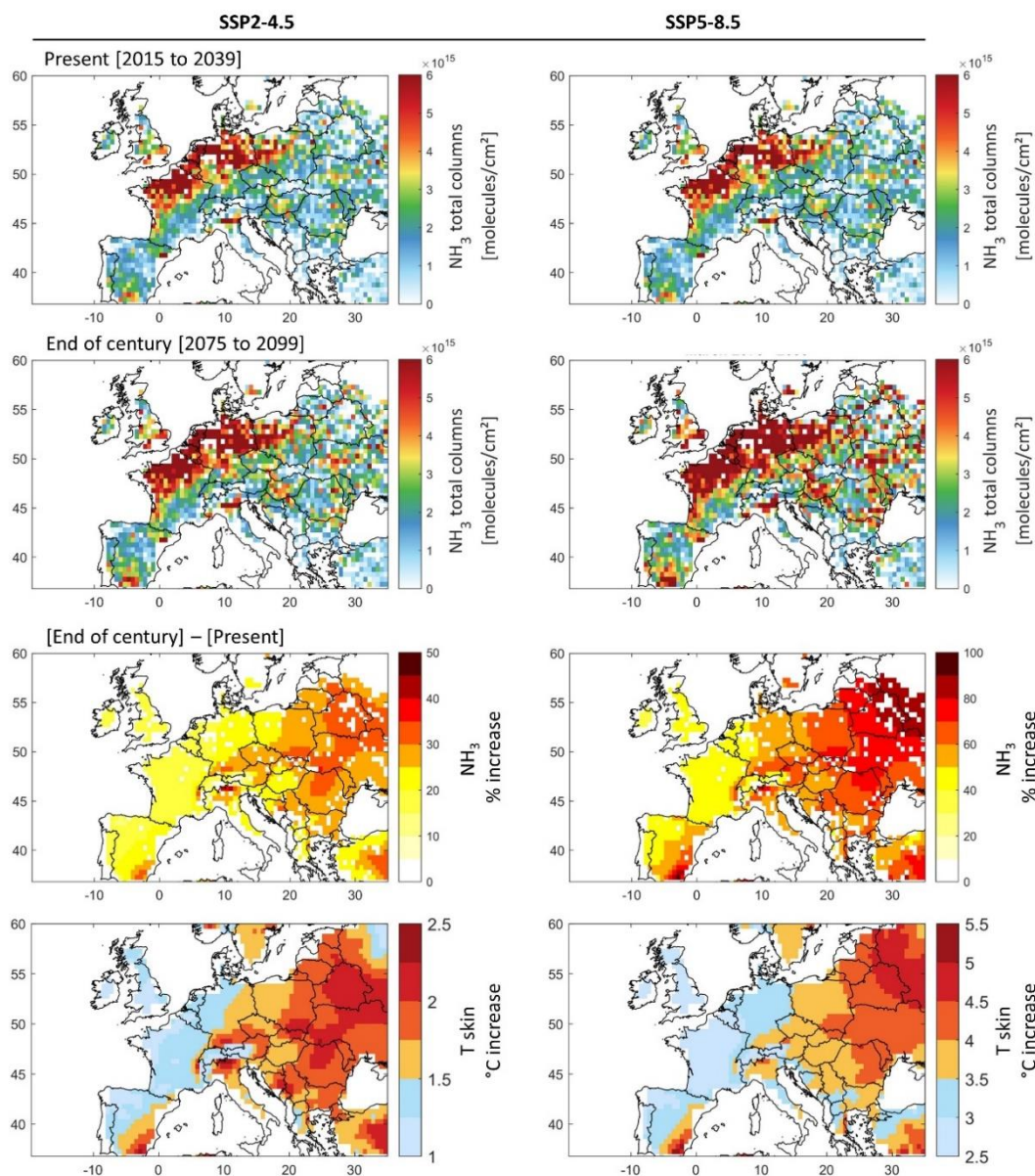| Region	Country	τ_{NH_3} [hours]	T skin [°C]			$\Gamma_{soil} \times 10^4$ [dimensionless]				NH$_3$ concentrations [molecules $\times 10^{15}$ cm^{-2}]		
			ERA5 IASI Overpass	ERA5	MERRA-2	Case 1	Case 2	Case 3	Case 4	IASI	GEOS-Chem	Mean MRD [%]
Ireland	Ireland	3.34	8.74	5.78	6.23	0.73	0.72	0.94	0.26	2.5	1.5	− 46
England	England	3.15	8.54	5.87	5.73	0.82	0.78	2.06	0.58	4.8	1.2	− 64
North European Plains	Belgium, Netherlands	5.16	7.46	4.93	4.57	1.86	1.71	2.51	1.00	7.7	3.9	− 49
Brittany	France	6.93	10.48	8.13	8.16	1.19	1.09	1.48	0.70	5.8	3.7	− 60
New Aquitaine	France	8.05	11.25	7.72	7.47	0.59	0.57	0.49	0.30	4.0	2.9	− 20
Po Valley	Italy	7.10	8.95	4.46	5.46	1.50	1.63	0.89	0.40	3.8	4.0	+ 110
Valladolid	Spain	4.53	11.64	6.87	6.93	0.55	0.55	0.62	0.20	2.5	1.3	− 42
Barcelona	Spain	4.94	12.61	7.05	9.44	0.43	0.46	0.65	0.28	3.2	1.5	− 49

5. Ammonia under future scenarios

Figure 7. First and second rows: Ammonia total column concentrations during March (monthly averages) under the present climate [2015 to 2039] (first row), and in the end of century climate [2075 to 2099] (second row), under the socio-economic scenarios SSP2-4.5 (left) and SSP5-8.5 (right). Third and fourth rows: The percentage increase in ammonia concentration (third row), and the change in T skin in °C (fourth row) by the end of the century [2075 to 2099] with respect to present climate [2015 to 2039] under SSP2-4.5 (left) and SSP5-8.5 (right). Ammonia columns were calculated using ammonia emission potential Γ_{soil} derived from IASI and ERA5 for March 2011 (case 3), and EC-Earth T skin simulations for SSP2-4.5 and SSP5-8.5 extending from 2015 till 2099.

465   As seen in Eq. (2-1), higher skin temperatures favour volatilization of ammonia from the soil. In an attempt to
466   understand how our simplified emission potential model behaves under changing climate, as well as under future
467   scenarios, we adopt the future T skin simulations from EC-Earth climate model, into Eq. (2-1). The two climate
468   socio-economic scenarios that we consider are SSP2-4.5 ("middle of the road" scenario where trends broadly
469   follow their historical patterns), and SSP5-8.5 (a world of rapid and unconstrained growth in economic output and
470   energy use) (Riahi et al., 2017). The same Figure constructed using Γ_{soil} from GEOS-Chem (case 1) is shown in
471   the supplementary material as Figure S5.
472   We calculate current and future ammonia columns assuming that the emission potential Γ_{soil} remains unchanged.
473   In other words, we assume that the same amount of fertilizers and manure is used until 2100 in the agricultural
474   fields and farms (unchanged ammonium soil content).
475   Figure 7 shows ammonia columns during the 25-year [2015 – 2039] representing the present climate (upper
476   panels), and the end of the century [2075 – 2099] (middle panels). The ammonia columns in the 25-year average
477   climate of the end of century with respect to present day climate (lower panels) are also shown.
478
479   Spatially, the present climate ammonia columns calculated from the T skin of the climate model and our emission
480   potential from IASI (case 3 in Figure 5), agree very well with those shown in Figure 1. We do not aim at validating
481   or directly comparing the two, as we are only interested in the climate response on ammonia concentration, i.e. by
482   the difference due to skin temperature increase (lower panels).
483
484   From Figure 7 (lower panels) it can be seen that the increase in ammonia columns by the end of the century is
485   more severe on the east side of Europe. Under the most likely scenario (SSP2-4.5), ammonia columns vary between
486   +15 % in France, to around +20 % in the North European Plain (Figure 7). The largest increase is detected in
487   Eastern Europe, where ammonia columns show an increase of up to a +50 % (Figure 7, lower left panels), creating
488   new potential hotspots/sources of ammonia in Belarus, Ukraine, Hungary, Moldova, parts of Romania and
489   Switzerland. Under the SSP5-8.5 scenario, the results show an increase in ammonia columns of up to +100 % in
490   Eastern Europe (Figure 7, right lower panel). This is directly related to the higher projected increase in skin
491   temperature over these regions. Other studies have equally reported Eastern Europe to be more affected by climate
492   change under future scenarios, as compared to western Europe (European Environment Energy, 2022; Jacob et al.,
493   2018). Spatially, the increase in ammonia coincides with the increase in T skin.
494   Figure 8 depicts the change in ammonia columns under the SSP2-4.5 and SSP5-8.5 scenarios, for our source
495   regions (shown as rectangles in Figure 2). Ammonia columns increase is foreseen to be the highest in the Po Valley
496   (Italy) with +26 % and +59 % under SSP2-4.5 and SSP5-8.5 respectively. It is then followed by the agricultural
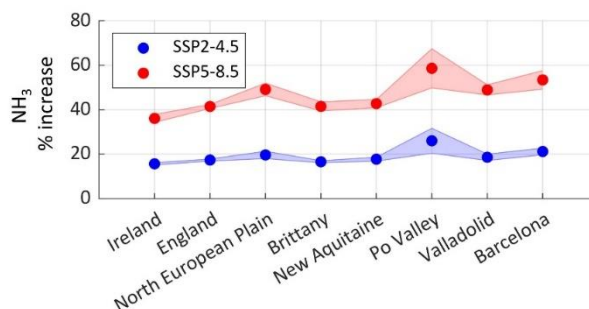

Figure 8. The percentage increase in ammonia concentration by the end of the century [2075 to 2099] with respect to the present climate [2015 to 2039] under the two climate scenarios SSP2-4.5 (blue) and SSP5-8.5 (red), in the source regions investigated in this study. The shades around each line represent the standard deviation from the mean.

497   areas around Barcelona (Spain), and the North European Plain (Belgium, Netherlands) with an increase of +21 %
498   (+49 %) and +20 % (+53 %) respectively, under the SSP2-4.5 (SSP5-8.5) scenario. Under the SSP5-8.5, the
499   increase in ammonia columns in percentage is more than twice the change under SSP2-4.5 (+127 % in the case of
500   the Po Valley for instance). The Po Valley is adjacent to the Alps mountains, and due to global warming, this
501   region is expected to experience increased evapotranspiration (Donnelly et al., 2017), which is a major factor that
502   leads to the volatilization of ammonia.
503   The local and regional effect of volatilization of ammonia under different climate scenarios remains difficult to be
504   properly assessed. Even under the "middle of the road" scenario 2-4.5, and without climate extremes (e.g.
505   heatwaves), Europe might be facing big challenges in air or downwind agricultural regions, since chemistry and
506   atmospheric transport (Figure 3) drive the loss of ammonia during the growing season in this part of the world.
507
508   An increase in ammonia concentration poses a significant and yet poorly understood effect on local and regional
509   air quality through the increase in $PM_{2.5}$ concentration. We note, however, that ammonia columns in the soil are
510   governed by a threshold. Higher temperatures will increase the rate of volatilization of ammonia from the soil, but
511   only up to a certain point where no dissolved ammonium is left. Plants, however, can also be a source of ammonia
512   when exposed to stressful conditions. For example, under heat stress and in instances where there are no ammonia
513   in the air, increase in air temperature results in exponential increase in ammonia emission from plants' leaves
514   (Husted and Schjoerring, 1996).

6.   Discussion and conclusions

515
516
517   Agriculture worldwide has fed the human race for thousands of years, and will continue to do so, as mankind
518   highly relies on it. Emissions from agricultural activities will inevitably increase, in order to meet the expected
519   yield. In this study, we use a variety of state-of-the-art datasets (satellite, reanalysis and model simulation) to
520   calculate the first regional map of ammonia emission potential during the start of the growing season in Europe.
521   The emission potential can be used as a proxy to calculate ammonia columns in the atmosphere, and as such to
522   assess its deposition, atmospheric transport, and contribution to PM formation. First, we show that the GEOS-
523   Chem chemistry transport model is able to reproduce key spatio-temporal patterns of ammonia levels over Europe.
524   The ammonia budget is governed by the emissions over source regions (North European Plain, Brittany and the
525   Po valley), as well as by key loss processes. We find that chemical loss pathway is responsible of 50 % or more of
526   the total ammonia loss over Europe. From the GEOS-Chem simulation, we calculate the average ammonia lifetime
527   in the atmosphere which ranges between 4 and 12 hours in agricultural source regions of Europe. From this, and
528   using the mass transfer coefficient for different land cover types, we calculate a range of emission potentials
529   Γ_{soil} from IASI and GEOS-Chem. We find that Γ_{soil} ranges between from 2×10^3 to 9.5×10^4 in fertilized lands
530   (croplands). Choosing a variable k from the literature, and based on different land cover types from MODIS, we
531   calculate Γ_{soil} values that are consistent with those found in the literature. The increase in T skin is expected to
532   have an effect on the emission of ammonia from the soil. Using T skin from the EC-Earth climate model, we
533   estimate ammonia columns by the end of the century [2075 – 2099], and compare it to columns of the present
534   climate [2015 – 2039]. Our results show that ammonia columns will double under the SSP5-8.5 scenario, and will
535   increase by up to 50 % under the most likely SSP2-4.5 scenario. The eastern part of Europe is the most affected
536   by the change in temperatures, and it is where we find the highest ammonia columns increase. Among the regions
537   of focus, Italy, Spain, Belgium and the Netherlands are the most affected, as compared to France, England and
538   Ireland. The highest increase in ammonia columns is observed in the Po Valley in Italy (+59 % under the SSP5-
539   8.5).
540

541 We calculate ammonia concentration under future climate and during the start of the growing season (March) in
542 Europe. However, in order to grasp the yearly budget of ammonia, it is crucial to apply this method to all seasons
543 of the year; especially in regions with extensive agricultural activities, such as the United States, India, and China.
544 In addition to this, more field measurements of ammonia emission potential (Γ_{soil}) in different land use / cover
545 types are required, this can help us perform better comparison with emission potentials calculated from model and
546 satellite data. Finally, having ammonia columns at different times of the day, from field observations or satellite
547 measurements will allow quantification of daily emission potentials, that will in turn help us understand its diurnal
548 variability. This will be ensured with the launch of the Infrared Sounder (IRS) on the Meteosat Third Generation
549 (MTG) geostationary satellites scheduled in 2025.

550

A. Appendix A

1. Ammonia-Ammonium equilibrium

Ammonia (NH_3) is a water-soluble gas, it undergoes protonation with H^+ from the hydronium ion H_3O^+ in an aqueous solution in order to give ammonium (NH_4^+ cation), the dissociation equation is expressed as follows:

(A-1)

$$NH_{3\,(aq)} + H_3O^+ \xrightarrow{K_{NH4+}} NH_{4\,(aq)}^+ + HO^-$$

555

Or

(A-2)

$$NH_{3\,(aq)} + H^+ \xrightarrow{K_{NH4+}} NH_{4\,(aq)}^+$$

557

With K_{NH4+} as the ammonium-ammonia dissociation equilibrium constant that can be expressed as:

$$K_{NH_4^+} = \frac{[NH_{3\,(aq)}][H^+]}{[NH_{4\,(aq)}^+]}$$

(A-3)

559
560

The solubility of ammonia in water is affected by the temperature and the acidity (pH) of the solvent (water). The equilibrium constant can be expressed as follows:

$$K_{NH_4+} = 5.67 \cdot 10^{-10} \exp\left[-6286 \left(\frac{1}{T} - \frac{1}{298.15}\right)\right]$$

(A-4)

563

2. Henry's equilibrium

Upon its dissolution in water, NH_3 obeys the Henry's law. Ammonia gas ($NH_{3\,(g)}$) near the surface of the solvent is in equilibrium with the dissolved ammonia in the aqueous phase $NH_{3\,(aq)}$ (in water). Henry's equilibrium is expressed as follows:

(A-5)

$$NH_{3\,(g)} \xrightarrow{H_{NH3}} NH_{3\,(aq)}$$

568

With H_{NH3} as the Henry's constant, it can be expressed as follows (Wichink Kruit, 2010):

$$H_{NH3} = \frac{[NH_{3\,(aq)}]}{[NH_{3\,(g)}]} = 5.527 \cdot 10^{-4} \cdot \exp\left[4092 \left(\frac{1}{T} - \frac{1}{298.15}\right)\right]$$

(A-6)

570

The partial pressure of ammonia near the surface of the soil can be calculated using Henry's constant and the dissociation equilibrium (Wichink Kruit, 2010):

$$P_{NH3} = \frac{K_{NH_4^+}[NH_4^+]}{H_{NH3}[H^+]} = \frac{5.67 \cdot 10^{-10} \cdot \exp\left[-6286\left(\frac{1}{T} - \frac{1}{298.15}\right)\right]}{5.527 \cdot 10^{-4} \cdot \exp\left[4092\left(\frac{1}{T} - \frac{1}{298.15}\right)\right]} \times \frac{[NH_4^+]}{[H^+]}$$

(A-7)

573

If we use the ideal gas law (PV=nRT), we can draw the link between the mass density of ammonia ($NH_{3\,(g)}$) and the partial pressure:

$$\chi_{NH_3} = \frac{P_{NH_3} \cdot M_{NH_3}}{R \cdot T} \qquad \text{(A-8)}$$

576

577 Where χ_{NH_3} is the concentration of NH$_3$ at the soil surface (kg m^{-3}), P_{NH3} is the partial pressure of NH$_3$ near the
578 surface (atm), M$_{NH3}$ is the molar mass of NH$_3$ (kg mol^{-1}), R is the gas constant (0.082 atm L mol^{-1} K^{-1}), and T is
579 the temperature in Kelvin.
580 Substituting Eq. (A-5) in (A-6) we get:

$$\chi_{NH_3} = \frac{2.75 \cdot 10^9 \left(\frac{gK}{m^3}\right)}{T_{soil}} \exp\left[\frac{-1.04 \cdot 10^4}{T_{soil}}\right] \Gamma_{soil} \qquad \text{(A-9)}$$

581

582 Where χ_{NH_3} is the concentration of ammonia at the soil surface at equilibrium (g m^{-3}), and is referred to as the
583 compensation point, T_{soil} is the temperature of the soil (Kelvin), Γ_{NH_3} is the NH$_3$ emission potential from the soil
584 and is a dimensionless ratio between [NH$_4^+$] and [H$^+$].

585 ### 3. Ammonia total columns from IASI

586 In this study we use the total columns of ammonia from IASI (molecules m^{-2}) in order to calculate the emission
587 potential Γ_{soil}, we should draw the link between these columns and this parameter. The bi-directional exchange of
588 NH$_3$ between the surface and the atmosphere can be expressed by the flux (assuming a flux independent of time)
589 (Roelle and Aneja, 2005; Zhang et al., 2010):

$$Flux_{NH_3} = k \left([NH_3]^{soil} - [NH_3]^{atm}\right) \qquad \text{(A-10)}$$

590

591 Where $Flux_{NH_3}$ is the bidirectional flux between the soil and the atmosphere (molecules (m² s)$^{-1}$), k is the soil –
592 atmosphere exchange velocity (m s^{-1}), also known as the mass transfer coefficient; $[NH_3]^{soil}$ is the concentration
593 of NH$_{3(g)}$ in the soil, and $[NH_3]^{atm}$ is the concentration of NH$_{3(g)}$ in the atmosphere (molecules m^{-3}).
594 Assuming a first order dissociation of NH$_3$, we can express the change in the $[NH_3]^{col}$ total columns as follows:

$$\frac{d[NH_3]^{col}}{dt} = Flux_{NH_3} - k'[NH_3]^{col} \qquad \text{(A-11)}$$

595

596 Where k' is the rate of dissociation of first order $k' = \frac{1}{\tau}$ (m s^{-1}), with τ the lifetime of NH$_3$ in the atmosphere.
597 Assuming steady state, and considering the $[NH_3]^{atm}$ as the $[NH_3]^{col}$, and $[NH_3]^{soil}$ as χ_{NH_3}, Eq. (A-9) can be
598 written as:

$$k \left(\frac{N_a \cdot \chi_{NH_3}}{M_{NH_3}} - \frac{1}{c}[NH_3]^{col}\right) = \frac{[NH_3]^{col}}{\tau} \qquad \text{(A-12)}$$

599

600 Where c is the column height and is equal to 6 km. It is important to note that we neglect the effect of transport by
601 wind since we only look at large regions. Finally, the total column of ammonia $[NH_3]^{col}$ can be written as:

$$[NH_3]^{col} = \frac{N_a \cdot \chi_{NH_3}}{M_{NH_3} \cdot \left(c + \frac{1}{k\tau}\right)} \qquad \text{(A-13)}$$

602

603 The column height is not considered anymore because it is negligible compared to $\frac{1}{k\tau}$, using Eq. (A-6) in (A-
604 11) we get:

$$[NH_3]^{col} = \frac{2.75 \cdot 10^{27} \left(\frac{gK}{cm^3}\right)}{T_{soil}} \exp\left[\frac{-1.04 \cdot 10^4}{T_{soil}}\right] \Gamma_{NH_3} \cdot k\tau \qquad \left(\frac{molecules}{cm^2}\right) \tag{A-14}$$

605

606 Note that $2.75 \cdot 10^{27} = \frac{a \cdot N_a \cdot c\prime}{M_{NH_3}} \left(\frac{K\ molecules}{cm^3}\right)$, where $a = 2.75 \cdot 10^3\ (g\ K\ cm^{-3})$, N_a Avogadro's number
607 (6.0221409×10^{23} molecules mol^{-1}), 10^{-2} is added to convert k from m s^{-1} to cm s^{-1}, and M_{NH_3} the molar mass of
608 NH$_3$ (17.031 g mol^{-1}). The emission potential of NH$_3$ from the soil can we written as:

$$\Gamma_{soil} = \frac{[NH_3]^{col} \cdot T_{soil}}{\exp(\frac{-b}{T_{soil}})} \frac{M_{NH_3}}{a \cdot N_a \cdot 10^{-2}} \cdot \frac{1}{k\tau} \tag{A-15}$$

609

610 Where $b = 1.04 \times 10^4\ K$.

Author contribution

RA contributed to the conception and design of the article, developed the code, wrote the manuscript, analysed and interpreted of the data, and approved the version for submission; CV, CC, and PFC revised the manuscript; WCP provided the GEOS-Chem simulation data, and revised the manuscript; NE provided ammonia lifetime calculation using the LMDz-OR-INCA chemistry transport model and commented on the manuscript; MVD and LC contributed to the acquisition of the IASI ammonia data (NH3-v3R-ERA5), and revised the manuscript; SS contributed to the conception and design of the article, provided the EC-Earth temperature data, and revised the manuscript, and approved the version for submission.

Acknowledgments

Funding information

Competing interests

The authors are aware of no competing interests.

Data accessibility statement

The IASI-NH$_3$ used in this study are retrieved from the Aeris data infrastructure (https://iasi.aeris-data.fr/nh3r-era5/). ERA5 skin temperature from 1979 to present are available for download in the following DOI: 10.24381/cds.adbb2d47. The GEOS-Chem outputs used in this study are only available upon request. EC-Earth3 model output prepared for CMIP6 ScenarioMIP are retrieved here: https://doi.org/10.22033/ESGF/CMIP6.727. The MODIS land cover data are available for download in the following link: https://doi.org/10.5067/MODIS/MCD12Q1.006.

References

Abeed, R., Clerbaux, C., Clarisse, L., Van Damme, M., Coheur, P.-F., and Safieddine, S. A space view of agricultural and industrial changes during the Syrian civil war. *Elem. Sci. Anthr.* https://doi.org/10.1525/elementa.2021.000041 (2021)

Adams, C., McLinden, C. A., Shephard, M. W., Dickson, N., Dammers, E., Chen, J., Makar, P., Cady-Pereira, K. E., Tam, N., Kharol, S. K., Lamsal, L. N., and Krotkov, N. A. Satellite-derived emissions of carbon monoxide, ammonia, and nitrogen dioxide from the 2016 Horse River wildfire in the Fort McMurray area. *Atmospheric Chem. Phys.* https://doi.org/10.5194/acp-19-2577-2019 (2019)

Alexander, B., Sherwen, T., Holmes, C. D., Fisher, J. A., Chen, Q., Evans, M. J., and Kasibhatla, P. Global inorganic nitrate production mechanisms: Comparison of a global model with nitrate isotope observations. *Atmospheric Chem. Phys.* https://doi.org/10.5194/acp-20-3859-2020 (2020)

Aneja, V. P., Rogers, H. H., and Stahel, E. P. Dry Deposition of Ammonia at Environmental Concentrations on Selected Plant Species. *J. Air Pollut. Control Assoc.* https://doi.org/10.1080/00022470.1986.10466183 (1986)

AQEG. *Fine particulate matter (PM2.5) in the United Kingdom* (p. 203). Air Quality Expert Group (AQEG), prepared for the Department for Environment, Food and Rural Affairs (Defra), Scottish Executive, Welsh Government and the Department of the Environment in Northern Ireland. https://uk-air.defra.gov.uk/assets/documents/reports/cat11/1212141150_AQEG_Fine_Particulate_Matter_in_the_UK.pdf (2012)

Barnes, A. P., Svensson, C., and Kjeldsen, T. R. North Atlantic air pressure and temperature conditions associated with heavy rainfall in Great Britain. *Int. J. Climatol.* https://doi.org/10.1002/joc.7414 (2022)

Bauer, S. E., Tsigaridis, K., and Miller, R. Significant atmospheric aerosol pollution caused by world food cultivation. *Geophys. Res. Lett.* https://doi.org/10.1002/2016GL068354 (2016)

Behera, S. N., Sharma, M., Aneja, V. P., and Balasubramanian, R. Ammonia in the atmosphere: A review on emission sources, atmospheric chemistry and deposition on terrestrial bodies. *Env. Sci Pollut Res*. https://doi.org/10.1007/s11356-013-2051-9 (2013)

Belward, A. S., Estes, John E., and Kline, K. D. The IGBP-DIS Global 1-Km Land-Cover Data Set DIS-Cover: A Project Overview. *Photogramm. Eng. Remote Sens.* https://www.asprs.org/wp-content/uploads/pers/1999journal/sep/1999_sept_1013-1020.pdf (1999)

Bey, I., Jacob, D. J., Yantosca, R. M., Logan, J. A., Field, B. D., Fiore, A. M., Li, Q., Liu, H. Y., Mickley, L. J., and Schultz, M. G. Global modeling of tropospheric chemistry with assimilated meteorology: Model description and evaluation. *J. Geophys. Res. Atmospheres.* https://doi.org/10.1029/2001JD000807 (2001)

Bouwman, A. F., Lee, D. S., Asman, W. a. H., Dentener, F. J., Van Der Hoek, K. W., and Olivier, J. G. J. A global high-resolution emission inventory for ammonia. *Glob. Biogeochem. Cycles.* https://doi.org/10.1029/97GB02266 (1997)

Clarisse, L., Van Damme, M., Clerbaux, C., and Coheur, P.-F. Tracking down global NH3 point sources with wind-adjusted superresolution. *Atmospheric Meas. Tech.* https://doi.org/10.5194/amt-12-5457-2019 (2019)

Clarisse, L., Van Damme, M., Gardner, W., Coheur, P.-F., Clerbaux, C., Whitburn, S., Hadji-Lazaro, J., and Hurtmans, D. Atmospheric ammonia (NH3) emanations from Lake Natron's saline mudflats. *Sci. Rep.* https://doi.org/10.1038/s41598-019-39935-3 (2019)

Clerbaux, C., Boynard, A., Clarisse, L., George, M., Hadji-Lazaro, J., Herbin, H., Hurtmans, D., Pommier, M., Razavi, A., Turquety, S., and Wespes, C. Monitoring of atmospheric composition using the thermal infrared IASI/MetOp sounder. *Atmospheric Chem. Phys.* https://doi.org/10.5194/acp-9-6041-2009 (2009)

Coheur, P.-F., Clarisse, L., Turquety, S., Hurtmans, D., and Clerbaux, C. IASI measurements of reactive trace species in biomass burning plumes. *Atmospheric Chem. Phys.* https://doi.org/10.5194/acp-9-5655-2009 (2009)

Dammers, E., McLinden, C. A., Griffin, D., Shephard, M. W., Van Der Graaf, S., Lutsch, E., Schaap, M., Gainairu-Matz, Y., Fioletov, V., Van Damme, M., Whitburn, S., Clarisse, L., Cady-Pereira, K., Clerbaux, C., Coheur, P. F., and Erisman, J. W. NH3 emissions from large point sources derived from CrIS and IASI satellite observations. *Atmospheric Chem. Phys.* https://doi.org/10.5194/acp-19-12261-2019 (2019)

693 David, M., Loubet, B., Cellier, P., Mattsson, M., Schjoerring, J. K., Nemitz, E., Roche, R., Riedo, M., and Sutton, M. A.
694   Ammonia sources and sinks in an intensively managed grassland canopy. *Biogeosciences*.
695   https://doi.org/10.5194/bg-6-1903-2009 (2009)
696 Donnelly, C., Greuell, W., Andersson, J., Gerten, D., Pisacane, G., Roudier, P., and Ludwig, F. Impacts of climate change on
697   European hydrology at 1.5, 2 and 3 degrees mean global warming above preindustrial level. *Clim. Change*.
698   https://doi.org/10.1007/s10584-017-1971-7 (2017)
699 Döscher, R., Acosta, M., Alessandri, A., Anthoni, P., Arneth, A., Arsouze, T., Bergmann, T., Bernadello, R., Bousetta, S.,
700   Caron, L.-P., Carver, G., Castrillo, M., Catalano, F., Cvijanovic, I., Davini, P., Dekker, E., Doblas-Reyes, F. J.,
701   Docquier, D., Echevarria, P., … Zhang, Q. The EC-Earth3 Earth System Model for the Climate Model
702   Intercomparison Project 6. *Geosci. Model Dev. Discuss.* https://doi.org/10.5194/gmd-2020-446 (2021)
703 ECMWF. *IFS Documentation CY43R1*. ECMWF. https://www.ecmwf.int/sites/default/files/elibrary/2016/17117-part-iv-
704   physical-processes.pdf (2016)
705 EDO, G. D. O. *Drought news in Europe: Situation in April 2011—Short Analysis of data from the European Drought
706   Observatory (EDO)* (p. 2). https://edo.jrc.ec.europa.eu/documents/news/EDODroughtNews201104.pdf (2011)
707 Erisman, J. W., Van Pul, A., and Wyers, P. Parametrization of surface resistance for the quantification of atmospheric
708   deposition of acidifying pollutants and ozone. *Atmos. Environ.* https://doi.org/10.1016/1352-2310(94)90433-2
709   (1994)
710 European Environment Energy. *Global and European temperatures*. https://www.eea.europa.eu/ims/global-and-european-
711   temperatures (2022)
712 Evangeliou, N., Balkanski, Y., Eckhardt, S., Cozic, A., Van Damme, M., Coheur, P.-F., Clarisse, L., Shephard, M., Cady-
713   Pereira, K., and Hauglustaine, D. 10-year satellite-constrained fluxes of ammonia improve performance of
714   chemistry transport models. *Atmospheric Chem. Phys.* https://doi.org/10.5194/acp-21-4431-2021 (2021)
715 Eyring, V., Bony, S., Meehl, G. A., Senior, C. A., Stevens, B., Stouffer, R. J., and Taylor, K. E. Overview of the Coupled
716   Model Intercomparison Project Phase 6 (CMIP6) experimental design and organization. *Geosci. Model Dev.*
717   https://doi.org/10.5194/gmd-9-1937-2016 (2016)
718 FAO. *FAO, GIEWS, Earth Observation*.
719   https://www.fao.org/giews/earthobservation/country/index.jsp?lang=enandcode=FRA (2022)
720 Flechard, C. R., Massad, R.-S., Loubet, B., Personne, E., Simpson, D., Bash, J. O., Cooter, E. J., Nemitz, E., and Sutton, M.
721   A. Advances in understanding, models and parameterizations of biosphere-atmosphere ammonia exchange.
722   *Biogeosciences*. https://doi.org/10.5194/bg-10-5183-2013 (2013)
723 Flechard, C. R., Nemitz, E., Smith, R. I., Fowler, D., Vermeulen, A. T., Bleeker, A., Erisman, J. W., Simpson, D., Zhang, L.,
724   Tang, Y. S., and Sutton, M. A. Dry deposition of reactive nitrogen to European ecosystems: A comparison of
725   inferential models across the NitroEurope network. *Atmospheric Chem. Phys.* https://doi.org/10.5194/acp-11-2703-
726   2011 (2011)
727 Flechard, C. R., Spirig, C., Neftel, A., and Ammann, C. The annual ammonia budget of fertilised cut grassland – Part 2:
728   Seasonal variations and compensation point modeling. *Biogeosciences*. https://doi.org/10.5194/bg-7-537-2010
729   (2010)
730 Folberth, G. A., Hauglustaine, D. A., Lathière, J., and Brocheton, F. Interactive chemistry in the Laboratoire de Météorologie
731   Dynamique general circulation model: Model description and impact analysis of biogenic hydrocarbons on
732   tropospheric chemistry. *Atmospheric Chem. Phys.* https://doi.org/10.5194/acp-6-2273-2006 (2006)
733 Garrido-Perez, J. M., Ordóñez, C., García-Herrera, R., and Barriopedro, D. Air stagnation in Europe: Spatiotemporal
734   variability and impact on air quality. *Sci. Total Environ.* https://doi.org/10.1016/j.scitotenv.2018.07.238 (2018)
735 Gelaro, R., McCarty, W., Suárez, M. J., Todling, R., Molod, A., Takacs, L., Randles, C. A., Darmenov, A., Bosilovich, M.
736   G., Reichle, R., Wargan, K., Coy, L., Cullather, R., Draper, C., Akella, S., Buchard, V., Conaty, A., Silva, A. M. da,
737   Gu, W., … Zhao, B. The Modern-Era Retrospective Analysis for Research and Applications, Version 2 (MERRA-
738   2). *J. Clim.* https://doi.org/10.1175/JCLI-D-16-0758.1 (2017)
739 Hersbach, H., Bell, B., Berrisford, P., Hirahara, S., Horányi, A., Muñoz-Sabater, J., Nicolas, J., Peubey, C., Radu, R.,
740   Schepers, D., Simmons, A., Soci, C., Abdalla, S., Abellan, X., Balsamo, G., Bechtold, P., Biavati, G., Bidlot, J.,
741   Bonavita, M., … Thépaut, J.-N. The ERA5 global reanalysis. *Q. J. R. Meteorol. Soc.*
742   https://doi.org/10.1002/qj.3803 (2020)

743 Hoesly, R. M., Smith, S. J., Feng, L., Klimont, Z., Janssens-Maenhout, G., Pitkanen, T., Seibert, J. J., Vu, L., Andres, R. J.,
744   Bolt, R. M., Bond, T. C., Dawidowski, L., Kholod, N., Kurokawa, J., Li, M., Liu, L., Lu, Z., Moura, M. C. P.,
745   O'Rourke, P. R., and Zhang, Q. Historical (1750–2014) anthropogenic emissions of reactive gases and aerosols
746   from the Community Emissions Data System (CEDS). *Geosci. Model Dev.* https://doi.org/10.5194/gmd-11-369-
747   2018 (2018)
748 Hourdin, F., Musat, I., Bony, S., Braconnot, P., Codron, F., Dufresne, J.-L., Fairhead, L., Filiberti, M.-A., Friedlingstein, P.,
749   Grandpeix, J.-Y., Krinner, G., LeVan, P., Li, Z.-X., and Lott, F. The LMDZ4 general circulation model: Climate
750   performance and sensitivity to parametrized physics with emphasis on tropical convection. *Clim. Dyn.*
751   https://doi.org/10.1007/s00382-006-0158-0 (2006)
752 Husted, S., and Schjoerring, J. K. Ammonia Flux between Oilseed Rape Plants and the Atmosphere in Response to Changes
753   in Leaf Temperature, Light Intensity, and Air Humidity (Interactions with Leaf Conductance and Apoplastic NH4+
754   and H+ Concentrations). *Plant Physiol.* https://doi.org/10.1104/pp.112.1.67 (1996)
755 Jacob, D., Kotova, L., Teichmann, C., Sobolowski, S. P., Vautard, R., Donnelly, C., Koutroulis, A. G., Grillakis, M. G.,
756   Tsanis, I. K., Damm, A., Sakalli, A., and van Vliet, M. T. H. Climate Impacts in Europe Under +1.5°C Global
757   Warming. *Earths Future.* https://doi.org/10.1002/2017EF000710 (2018)
758 Keller, C. A., Long, M. S., Yantosca, R. M., Da Silva, A. M., Pawson, S., and Jacob, D. J. HEMCO v1.0: A versatile,
759   ESMF-compliant component for calculating emissions in atmospheric models. *Geosci. Model Dev.*
760   https://doi.org/10.5194/gmd-7-1409-2014 (2014)
761   Klaes, K. D. The EUMETSAT Polar System. *Comprehensive Remote Sensing.* Elsevier.
762   https://doi.org/10.1016/B978-0-12-409548-9.10318-5 (2018)
763 Krinner, G., Viovy, N., de Noblet-Ducoudré, N., Ogée, J., Polcher, J., Friedlingstein, P., Ciais, P., Sitch, S., and Prentice, I.
764   C. A dynamic global vegetation model for studies of the coupled atmosphere-biosphere system. *Glob. Biogeochem.*
765   *Cycles.* https://doi.org/10.1029/2003GB002199 (2005)
766 Lee, W., An, S., and Choi, Y. Ammonia harvesting via membrane gas extraction at moderately alkaline pH: A step toward
767   net-profitable nitrogen recovery from domestic wastewater. *Chem. Eng. J.*
768   https://doi.org/10.1016/j.cej.2020.126662 (2020)
769 Lentze, G. *Metop-A satellite retiring after 15 years of huge benefits to forecasting* [Text]. *ECMWF.* ECMWF.
770   https://www.ecmwf.int/en/about/media-centre/news/2021/metop-satellite-retiring-after-15-years-huge-benefits-
771   forecasting (2021, November 12)
772 Luo, Z., Zhang, Y., Chen, W., Van Damme, M., Coheur, P.-F., and Clarisse, L. Estimating global ammonia (NH_3)
773   emissions based on IASI observations from 2008 to 2018. *Atmospheric Chem. Phys.* https://doi.org/10.5194/acp-22-
774   10375-2022 (2022)
775 Massad, R.-S., Nemitz, E., and Sutton, M. A. Review and parameterisation of bi-directional ammonia exchange between
776   vegetation and the atmosphere. *Atmospheric Chem. Phys.* https://doi.org/10.5194/acp-10-10359-2010 (2010)
777 Masson-Delmotte, V., P. Zhai, A. Pirani, S.L., Connors, C. Péan, S. Berger, N. Caud, Y. Chen, L. Goldfarb, M.I. Gomis, M.
778   Huang, K. Leitzell, E. Lonnoy, J.B.R., and Matthews, T.K. Maycock, T. Waterfield, O. Yelekçi, R. Yu, and B.
779   Zhou. *IPCC, 2021: Climate Change 2021: The Physical Science Basis. Contribution of Working Group I to the*
780   *Sixth Assessment Report of the Intergovernmental Panel on Climate Change.* Cambridge University Press. In Press.
781   https://www.ipcc.ch/assessment-report/ar6/ (2021)
782 Mattsson, M., B, H., M, D., Loubet, B., M, R., Theobald, M., Sutton, M., Bruhn, D., Neftel, A., and Schjoerring, J. Temporal
783   variability in bioassays of ammonia emission potential in relation to plant and soil N parameters in intensively
784   managed grassland. *Biogeosciences Discuss.* https://doi.org/10.5194/bgd-5-2749-2008 (2008)
785 McDuffie, E. E., Smith, S. J., O'Rourke, P., Tibrewal, K., Venkataraman, C., Marais, E. A., Zheng, B., Crippa, M., Brauer,
786   M., and Martin, R. V. A global anthropogenic emission inventory of atmospheric pollutants from sector- and fuel-
787   specific sources (1970–2017): An application of the Community Emissions Data System (CEDS). *Earth Syst. Sci.*
788   *Data.* https://doi.org/10.5194/essd-12-3413-2020 (2020)
789 Met Office. *Exceptionally warm and dry Spring 2011.* Met Office.
790   https://www.metoffice.gov.uk/binaries/content/assets/metofficegovuk/pdf/weather/learn-about/uk-past-
791   events/interesting/2011/exceptionally-warm-and-dry-spring-2011---met-office.pdf (2016)

792 Nemitz, E., Sutton, M. A., Schjoerring, J. K., Husted, S., and Paul Wyers, G. Resistance modelling of ammonia exchange
793   over oilseed rape. *Agric. For. Meteorol.* https://doi.org/10.1016/S0168-1923(00)00206-9 (2000)
794 Olesen, J. E., and Sommer, S. G. Modelling effects of wind speed and surface cover on ammonia volatilization from stored
795   pig slurry. *Atmospheric Environ. Part Gen. Top.* https://doi.org/10.1016/0960-1686(93)90030-3 (1993)
796 Personne, E., Tardy, F., Génermont, S., Decuq, C., Gueudet, J.-C., Mascher, N., Durand, B., Masson, S., Lauransot, M.,
797   Fléchard, C., Burkhardt, J., and Loubet, B. Investigating sources and sinks for ammonia exchanges between the
798   atmosphere and a wheat canopy following slurry application with trailing hose. *Agric. For. Meteorol.*
799   https://doi.org/10.1016/j.agrformet.2015.03.002 (2015)
800 Phillips, S. B., Arya, S. P., and Aneja, V. P. Ammonia flux and dry deposition velocity from near-surface concentration
801   gradient measurements over a grass surface in North Carolina. *Atmos. Environ.*
802   https://doi.org/10.1016/j.atmosenv.2004.02.054 (2004)
803 Pinder, R. W., Gilliland, A. B., and Dennis, R. L. Environmental impact of atmospheric NH3 emissions under present and
804   future conditions in the eastern United States. *Geophys. Res. Lett.* https://doi.org/10.1029/2008GL033732 (2008)
805 Plumb, R. A., and Stolarski, R. S. Chapter 2: The Theory of Estimating Lifetimes Using Models and Observations. *SPARC*
806   *Lifetimes Rep. 2013 – SPARC Rep. No 6.* https://pages.jh.edu/rstolar1/other_pubs/LifetimeReport_Ch2.pdf (2013)
807 Potapov, P., Turubanova, S., Hansen, M. C., Tyukavina, A., Zalles, V., Khan, A., Song, X.-P., Pickens, A., Shen, Q., and
808   Cortez, J. Global maps of cropland extent and change show accelerated cropland expansion in the twenty-first
809   century. *Nat. Food.* https://doi.org/10.1038/s43016-021-00429-z (2022)
810 Randerson, J. T., Van Der Werf, G. R., Giglio, L., Collatz, G. J., and Kasibhatla, P. S. Global Fire Emissions Database,
811   Version 4.1 (GFEDv4). *ORNL DAAC.* https://doi.org/10.3334/ORNLDAAC/1293 (2015)
812 Riahi, K., van Vuuren, D. P., Kriegler, E., Edmonds, J., O'Neill, B. C., Fujimori, S., Bauer, N., Calvin, K., Dellink, R.,
813   Fricko, O., Lutz, W., Popp, A., Cuaresma, J. C., Kc, S., Leimbach, M., Jiang, L., Kram, T., Rao, S., Emmerling, J.,
814   … Tavoni, M. The Shared Socioeconomic Pathways and their energy, land use, and greenhouse gas emissions
815   implications: An overview. *Glob. Environ. Change.* https://doi.org/10.1016/j.gloenvcha.2016.05.009 (2017)
816 Roelle, P. A., and Aneja, V. P. Modeling of Ammonia Emissions from Soils. *Environ. Eng. Sci.*
817   https://doi.org/10.1089/ees.2005.22.58 (2005)
818 Schlesinger, W. H., and Hartley, A. E. A global budget for atmospheric NH3. *Biogeochemistry.*
819   https://doi.org/10.1007/BF00002936 (1992)
820 Shen, H., Chen, Y., Hu, Y., Ran, L., Lam, S. K., Pavur, G. K., Zhou, F., Pleim, J. E., and Russell, A. G. Intense Warming
821   Will Significantly Increase Cropland Ammonia Volatilization Threatening Food Security and Ecosystem Health.
822   *One Earth.* https://doi.org/10.1016/j.oneear.2020.06.015 (2020)
823 Shephard, M. W., and Cady-Pereira, K. E. Cross-track Infrared Sounder (CrIS) satellite observations of tropospheric
824   ammonia. *Atmos Meas Tech.* https://doi.org/10.5194/amt-8-1323-2015 (2015)
825 Sulla-Menashe, D., and Friedl, M. A. *User Guide to Collection 6 MODIS Land Cover (MCD12Q1 and MCD12C1) Product.*
826   https://lpdaac.usgs.gov/documents/101/MCD12_User_Guide_V6.pdf (2018)
827 Svensson, L., and Ferm, M. Mass Transfer Coefficient and Equilibrium Concentration as Key Factors in a New Approach to
828   Estimate Ammonia Emission from Livestock Manure. *J. Agric. Eng. Res.* https://doi.org/10.1006/jaer.1993.1056
829   (1993)
830 Theobald, M. R., Crittenden, P. D., Hunt, A. P., Tang, Y. S., Dragosits, U., and Sutton, M. A. Ammonia emissions from a
831   Cape fur seal colony, Cape Cross, Namibia. *Geophys. Res. Lett.* https://doi.org/10.1029/2005GL024384 (2006)
832 Tournadre, B., Chelin, P., Ray, M., Cuesta, J., Kutzner, R. D., Landsheere, X., Fortems-Cheiney, A., Flaud, J.-M., Hase, F.,
833   Blumenstock, T., Orphal, J., Viatte, C., and Camy-Peyret, C. Atmospheric ammonia (NH3 over the Paris megacity:
834   9 years of total column observations from ground-based infrared remote sensing. *Atmospheric Meas. Tech.*
835   https://doi.org/10.5194/amt-13-3923-2020 (2020)
836 USDA. *Europe—Crop Calendars. Foreign Agric. Serv. US Dep. Agric.* Foreign Agricultural Service, U.S. Department of
837   Agriculture. https://ipad.fas.usda.gov/rssiws/al/crop_calendar/europe.aspx (2022, May 12)
838 Van Damme, M., Clarisse, L., Franco, B., Sutton, M. A., Erisman, J. W., Wichink Kruit, R., van Zanten, M., Whitburn, S.,
839   Hadji-Lazaro, J., Hurtmans, D., Clerbaux, C., and Coheur, P.-F. Global, regional and national trends of atmospheric
840   ammonia derived from a decadal (2008-2018) satellite record. *Environ. Res. Lett.* https://doi.org/10.1088/1748-
841   9326/abd5e0 (2021)

842 Van Damme, M., Clarisse, L., Whitburn, S., Hadji-Lazaro, J., Hurtmans, D., Clerbaux, C., and Coheur, P.-F. Industrial and
843   agricultural ammonia point sources exposed. *Nature*. https://doi.org/10.1038/s41586-018-0747-1 (2018)
844 Van Damme, M., Whitburn, S., Clarisse, L., Clerbaux, C., Hurtmans, D., and Coheur, P.-F. Version 2 of the IASI NH3
845   neural network retrieval algorithm; near-real time and reanalysed datasets. *Atmos. Meas. Tech.,* 10, 4905–4914,
846   https://doi.org/10.5194/amt-10-4905-2017 (2017)
847 Van Der Molen, J., Beljaars, A. C. M., Chardon, W. J., Jury, W. A., and Faassen, H. G. van. Ammonia volatilization from
848   arable land after application of cattle slurry. 2. Derivation of a transfer model. *Neth. J. Agric. Sci.*
849   https://doi.org/10.18174/njas.v38i3A.16586 (1990)
850 Viatte, C., Abeed, R., Yamanouchi, S., Porter, W., Safieddine, S., Van Damme, M., Clarisse, L., Herrera, B., Grutter, M.,
851   Coheur, P.-F., Strong, K., and Clerbaux, C. NH$_3$ spatio-temporal variability over Paris, Mexico and Toronto and its
852   link to PM$_{2.5}$ during pollution events. *EGUsphere*. https://doi.org/10.5194/egusphere-2022-413 (2022)
853 Viatte, C., Petit, J.-E., Yamanouchi, S., Van Damme, M., Doucerain, C., Germain-Piaulenne, E., Gros, V., Favez, O.,
854   Clarisse, L., Coheur, P.-F., Strong, K., and Clerbaux, C. Ammonia and PM2.5 Air Pollution in Paris during the
855   2020 COVID Lockdown. *Atmosphere*. https://doi.org/10.3390/atmos12020160 (2021)
856 Viatte, C., Wang, T., Van Damme, M., Dammers, E., Meleux, F., Clarisse, L., Shephard, M. W., Whitburn, S., Coheur, P. F.,
857   Cady-Pereira, K. E., and Clerbaux, C. Atmospheric ammonia variability and link with particulate matter formation:
858   A case study over the Paris area. *Atmospheric Chem. Phys.* https://doi.org/10.5194/acp-20-577-2020 (2020)
859 Wentworth, G. R., Murphy, J. G., Gregoire, P. K., Cheyne, C. A. L., Tevlin, A. G., and Hems, R. Soil–atmosphere exchange
860   of ammonia in a non-fertilized grassland: Measured emission potentials and inferred fluxes. *Biogeosciences*.
861   https://doi.org/10.5194/bg-11-5675-2014 (2014)
862 Wesely, M. L. Parameterization of surface resistances to gaseous dry deposition in regional-scale numerical models.
863   *Atmospheric Environ. 1967*. https://doi.org/10.1016/0004-6981(89)90153-4 (1989)
864 Whitburn, S., Damme, M. V., Clarisse, L., Bauduin, S., Heald, C. L., Hadji-Lazaro, J., Hurtmans, D., Zondlo, M. A.,
865   Clerbaux, C., and Coheur, P.-F. A flexible and robust neural network IASI-NH3 retrieval algorithm. *J. Geophys.*
866   *Res. Atmospheres*. https://doi.org/10.1002/2016JD024828 (2016)
867 Wichink Kruit, R. Surface-atmosphere exchange of ammonia. Ph.D., Wageningen University. Wageningen, Netherlands,
868   https://edepot.wur.nl/137586 (2010)
869 Yang, S., Yuan, B., Peng, Y., Huang, S., Chen, W., Hu, W., Pei, C., Zhou, J., Parrish, D. D., Wang, W., He, X., Cheng, C.,
870   Li, X.-B., Yang, X., Song, Y., Wang, H., Qi, J., Wang, B., Wang, C., … Shao, M. The formation and mitigation of
871   nitrate pollution: Comparison between urban and suburban environments. *Atmospheric Chem. Phys.*
872   https://doi.org/10.5194/acp-22-4539-2022 (2022)
873 Yu, F., Nair, A. A., and Luo, G. Long-Term Trend of Gaseous Ammonia Over the United States: Modeling and Comparison
874   with Observations. *J. Geophys. Res. Atmospheres*. https://doi.org/10.1029/2018JD028412 (2018)
875 Zhang, L., Wright, L. P., and Asman, W. a. H. Bi-directional air-surface exchange of atmospheric ammonia: A review of
876   measurements and a development of a big-leaf model for applications in regional-scale air-quality models. *J.*
877   *Geophys. Res. Atmospheres*. https://doi.org/10.1029/2009JD013589 (2010)
878